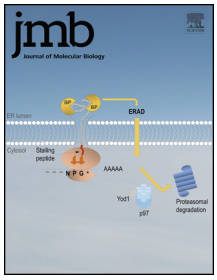

The N-Terminal Segment of the Voltage-Dependent Anion Channel: A Possible Membrane-Bound Intermediate in Pore Unbinding

Maria M. Reif [1], Moritz Fischer [1], Kai Fredriksson [2], Franz Hagn [2,3] and Martin Zacharias [1]

*1 - **Physics Department (T38),** Technische Universität München, James-Franck-Str. 1, D-85748 Garching, Germany*
*2 - **Laboratory of Structural Membrane Biochemistry,** Bavarian NMR Center, Institute for Advanced Study, Technische Universität München, Ernst-Otto-Fischer-Str. 2, D-85748 Garching, Germany*
*3 - **Institute of Structural Biology,** Helmholtz Zentrum München, Ingolstädter Landstr. 1, D-85764 Neuherberg, Germany*

***Correspondence to Maria M. Reif:** maria.reif@tum.de.*
https://doi.org/10.1016/j.jmb.2018.09.015
Edited by Anna Panchenko

Abstract

The voltage-dependent anion channel (VDAC) resides in the outer mitochondrial membrane and can adopt a closed or open configuration, most likely depending on whether the N-terminal segment (NTS) occupies the pore or protrudes into the cytoplasm. In this study, we calculate the free energy of releasing the NTS from the pore using molecular dynamics simulation. This is complicated by the flexible nature of the NTS, in particular its disordered structure in aqueous solution compared to the pore lumen. We carried out potential of mean force calculations using enhanced sampling or conformational restraints to address the conformational sampling problem. For the binding to the VDAC pore, two systems were considered, featuring either the native VDAC system or a modified system where the NTS is detached from the pore, that is, noncovalently bound in the pore lumen. The calculated free energies required to translocate the NTS from the pore into the solvent moiety are 83.8 or 74.3 kJ mol^{-1}, respectively. The dissociation pathway in VDAC presents two in-pore minima, separated by a low free energy barrier and a membrane-bound intermediate state. Since we observe small changes in pore shape along the NTS dissociation pathway, we suggest that rigidification of the VDAC pore might impair NTS dissociation. The stability of the membrane-bound state of the VDAC NTS is confirmed by independent molecular dynamics simulations showing spontaneous membrane binding of a NTS-derived peptide as well as nuclear magnetic resonance experiments where chemical shift perturbations of the NTS-derived peptide evidence binding to phospholipid nanodiscs.

Introduction

The voltage-dependent anion channel (VDAC) is an extensively studied protein [1–5], yet many aspects of it remain enigmatic. One major reason for the complexity associated with VDAC is its special location in the outer mitochondrial membrane (OMM) [6,7] and the important functions VDAC is associated with as a "gatekeeper of life and death" [6]. As such, it controls the flow of metabolites and the reaction of cells to environmental stress. The abundance of VDAC in the OMM and the role it plays in physiology and various diseases [2,8,9] further emphasize its importance. The primary function of VDAC is voltage-dependent gating. In the open state, VDAC is anion selective, whereas it is slightly cation selective in the closed state [10]. The underlying control mechanism is voltage sensing, that is, the cation selectivity (albeit at a rather low conductance) is induced when a high negative or positive voltage (> 30 mV magnitude) is applied.

In the following, VDAC refers to the VDAC1 isoform of the protein in humans. X-ray [11] (PDB ID 3EMN; 2.3 Å resolution) and NMR [12] (PDB ID 2K4T) structures of VDAC are available. Both present a β-barrel pore composed of 19 β-strands. The N-terminal segment (NTS) of the protein is not included in the barrel architecture but protrudes into the pore. While the x-ray structure reveals a helical NTS (3_{10}-helix for residues T6-K12; α-helix for residues S13-K20), this is not resolved by the NMR structure. In the latter, the NTS is rather disordered,

indicating its flexible nature. The isolated NTS was found to adopt a helical conformation in apolar environments [13,14] and detergents [15], whereas it is unstructured in water [15].

The NTS of VDAC appears to play a vital role in cell metabolism. Many research questions focus on the NTS, for example, concerning the control of gating or of pore conformation or its involvement in oligomerization, binding to ATP or to apoptosis-regulating proteins [4,16]. However, considering the typical structure–function relationship required to fully characterize the workings of a protein, our understanding of VDAC is already limited in the very basics, the structural features of the VDAC NTS [4,16]. It appears that its flexible nature is restricted not only to secondary structure (see above) but also concerns its location. Studies suggest that it may reside in the pore lumen [4,11,12,17], in the cytoplasm [15] or at the membrane surface [18]. A second ambiguity affects VDAC dimerization, with some evidence suggesting that the NTS leaves the pore lumen and mutual interaction of these segments in the cytoplasmic region facilitates dimerization [19], while the contrary (i.e., insignificance of the NTS for VDAC association) has also been suggested [20]. Third, it is not clear whether the NTS is involved in voltage gating [5,21], and, if yes, how. Again, the NTS may be mobile [1,4] or stay within the pore lumen [3,17,22]. It might also be that the shape of the barrel is important for gating, that is, the closed state being a partially collapsed barrel, with the NTS stabilizing the open state [23]. Further complexity might be due to membrane composition affecting the barrel and hence gating [16,24,25].

Previous molecular dynamics (MD) studies of VDAC have focused on the voltage dependence of the pore conformation and selectivity [21], ATP transport through the pore [26], and the effect of mutation of E73 on pore dynamics [27] or of deletion of the NTS on pore conformation [23]. Up to now, no MD studies have been performed on the dissociation of the NTS from the VDAC pore. Thermodynamic characterization of this process is of interest to draw conclusions about the location of the NTS, for example, to answer questions such as whether the NTS can spontaneously leave the pore or whether the NTS can adopt alternative low-free energy positions within the pore. The gained knowledge can, in turn, support our understanding of VDAC function. We performed extensive MD simulations to characterize dissociation of the NTS from the pore lumen *via* potential of mean force (PMF) calculations. Our goals were to assess whether spontaneous dissociation of the NTS from the pore lumen is possible and to characterize possible free-energy minima along the dissociation pathway of the NTS out of the pore lumen. Our simulations indicate that (i) the NTS does not spontaneously leave the pore, as *ca.* 45 (covalently attached NTS) or 35 kJ mol^{-1} (noncovalently attached NTS) are required to remove the NTS from the VDAC pore and install it in a position outside the pore near the membrane headgroup region; (ii) a further *ca.* 40 kJ mol^{-1} is required to detach the NTS and immerse it in the bulk; (iii) the NTS may adopt other (non-native; here meaning different than in the x-ray structure) positions within the pore, although only the x-ray-structure like position was observed during a free 80-ns simulation; (iv) the NTS may adopt a stable membrane-bound state along the dissociation pathway.

To gain evidence for a preference of membrane attachment of the NTS in comparison to the solvated state, we performed NMR experiments and analyzed chemical shift perturbations (CSPs) associated with addition of phospholipid nanodiscs to solvated NTS-derived peptides. The observed CSPs give clear evidence for binding of the peptide to the nanodiscs, which confirms favorable membrane attachment of the solvated VDAC NTS-derived peptide. Finally, we performed additional MD simulations to corroborate spontaneous association of the peptide with a phospholipid bilayer. This involved free simulations starting from a solvated peptide, which showed spontaneous membrane binding as well as the calculation of a PMF of peptide–membrane attachment. So far, only indirect biochemical evidence for membrane binding of the VDAC NTS was available [18] through an immunofluorescence study employing antibodies against the VDAC NTS. However, from this study, it is still unclear whether the antibodies bind to an already exposed VDAC NTS outside the pore lumen or whether antibody–VDAC NTS association influences attachment of the NTS to the membrane.

To our knowledge, the present work is the first study providing quantitative insight into the thermodynamics of VDAC NTS dissociation from the pore lumen and into the structural and thermodynamic features of a VDAC NTS membrane complex, as well as direct experimental evidence for association of a solvated NTS-derived peptide with a phospholipid membrane.

Results and Discussion

Structural characteristics of VDAC wild type and mutants V143A and L150A

During the course of 80-ns production simulations, the NTS adopts a stable position in the wild type and the two mutants V143A and L150A (Fig. 1). No transitions of the NTS to other positions are observed on the simulated timescale. The orientation of the NTS is similar in the wild type and the mutants (mean angles θ formed with the membrane normal of 103.9, 101.6 and 102.3 deg. in simulations wt, V143A and L150A, respectively). The fluctuation in the distance between barrel com and NTS com is

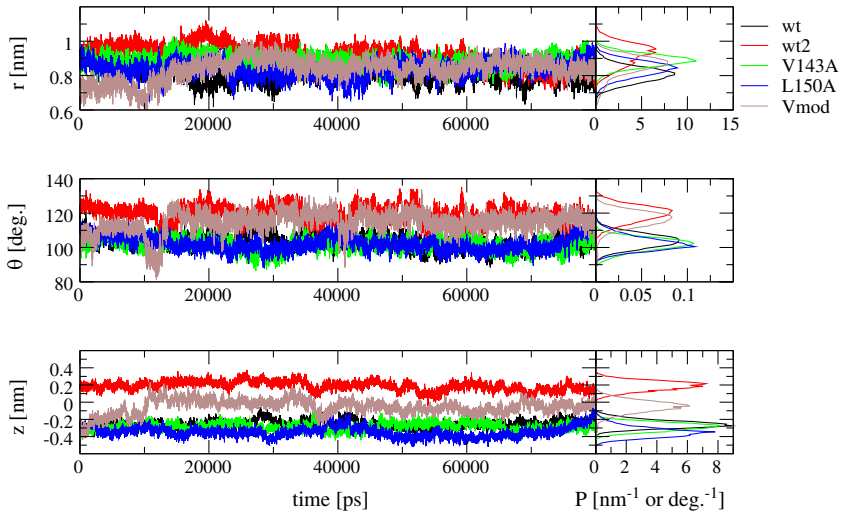

Fig. 1. Time series and probability distributions for the distance r between the com of heavy atoms of the beta barrel (residues 27–283) and the com of the NTS backbone (residues 8–19), the z-coordinate z of the corresponding distance vector and the angle θ between the z-axis and the vector connecting the C_α atoms of NTS residues 9 and 18. The data is depicted for systems wt, wt2, V143A, L150A and Vmod. For the latter, the time series panels do not depict the last 40 ns, but the probability distributions refer to the full 120 ns sampling time. Simulation acronyms are explained in Table 1.

also similar (standard deviations of 0.05, 0.04 and 0.05 nm in simulations wt, V143A and L150, respectively). The NTS also adopts a rather stable secondary structure in all simulations (Table 2). The fraction of helical (including α-, 3_{10}- and π-helix) structure is very similar in the wild type and mutant systems.

Figure S3 depicts the angles φ enclosed by the major axes of ellipses fit to the β-barrel and the x-axis. The mutant systems each show two pronounced maxima in the φ distribution (less pronounced in V143A than in L150A), whereas there is only one pronounced maximum in the wt system. Thus, the ellipse tends to deform in a distinct fashion in the mutant systems. Note that a "breathing" motion of the ellipse would be indicated by maxima that are separated by about 90 deg., that is, an exchange of minor and major axes. This is seen to a

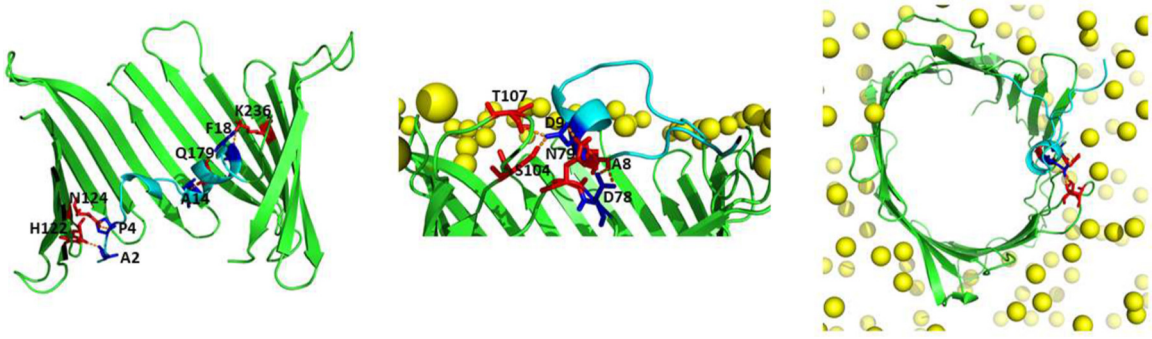

(a) (b) (c)

Fig. 2. Cartoon representations of VDAC with selected residues shown in stick representation to illustrate hydrogen bonds. In panels b and c, phosphorus atoms of the membrane are shown as yellow spheres. Important hydrogen bonds between the beta barrel (residues 27–283) and residues 1–20 are depicted as dashed orange lines. (a) Hydrogen bonds occurring more than 50% of the simulation time in system wt. The hydrogen bonds are reported in Table 3. (b) Selected hydrogen bonds occurring more than 30% of the simulation time in plateau region (2) of PMF1 (Fig. 4), that is, where the NTS lies outside the pore opening. The depicted hydrogen bonds are A8 NH with D78 OD1 and OD2, N79 HD21 with D9 OD1, S104 HG with D9 OD2 and T107 HG1 with D9 OD2. (c) As panel b, but top view onto the barrel. Simulation acronyms are explained in Table 1.

certain extent in L150A. Note also that the relative position of the maxima may not be compared among the different systems because the β-barrels were not fit to the same structure.

Important hydrogen bonds between the NTS and the barrel moiety are reported in Table 3 and depicted in Fig. 2a. The very stable hydrogen bond between the backbones of A2 and H122 present in simulation wt with an occurrence of 91.9% is present with reduced occurrences in the V143A (55.5%) and L150A (63.3%) mutants. The hydrogen bond involving K236 and F18 is absent in both mutants. The location of the point mutations in the mutant systems is illustrated in Fig. 3a. V143 and L150 are in neighboring β-strands, in the lower half of the barrel, that is, close to the mitochondrial intermembrane space. Both VDAC variants showed lower yields in refolding experiments, suggesting a weaker NTS–barrel interaction required for adopting a stable tertiary structure (F. Hagn, personal communication, 2016). The only observation in the present simulations compatible with this is the reduced occurrence of stabilizing hydrogen bond interactions in these systems. Secondary structure stability and location of the NTS in the mutants are overall rather similar to the wt system. To summarize, structural differences between wt and the mutant species mainly concern barrel shape characteristics and hydrogen bond interactions between the NTS and the barrel moiety.

Binding of the NTS to VDAC

We carried out PMF calculations to investigate whether spontaneous dissociation of the VDAC NTS from the pore lumen is possible. Figures 4a and b provide the free-energy profiles for the dissociation pathway in the VDAC wild type and the modified protein with a noncovalently bound NTS-derived peptide, respectively. The former shows the following:

(A) In-barrel minima 0.22 nm below and 0.17–0.22 nm above the barrel com, separated by a free-energy barrier of 6.2 kJ mol^{-1} (2.5 k_BT at 300 K), measured with respect to the first minimum. Transitions between alternative positions of the NTS along the membrane normal were not observed during the free simulations. Note that the former minimum corresponds to the x-ray structure 3EMN (Fig. 1). Structural features of the two systems are discussed in the Structural characteristics of VDAC wild type and mutants V143A and L150A and Structural characteristics of VDAC in the wt2 position and comparison with Vmod sections.

(B) Plateau regions at 0.85–1.11 nm and 1.47–2.00 nm above the barrel com. They are highlighted in Fig. 4a, with labels (1) and (2), respectively, at their centers. Representative snapshots are shown in Fig. 5a, d, and b, e, respectively. The former region is characterized by a rather stable hydrogen bond between the side chain amine group of N185 and the backbone oxygen of P5, on average present during 72.1% of the simulation time in the concerned PMF windows. The secondary structure content of the NTS is still akin to that in the native position (Fig. 6). The second plateau region lies outside the pore opening and captures the membrane-bound NTS intermediate. The most important NTS–barrel hydrogen bond interactions in this region, present more than 30% of the simulation time in either of the concerned

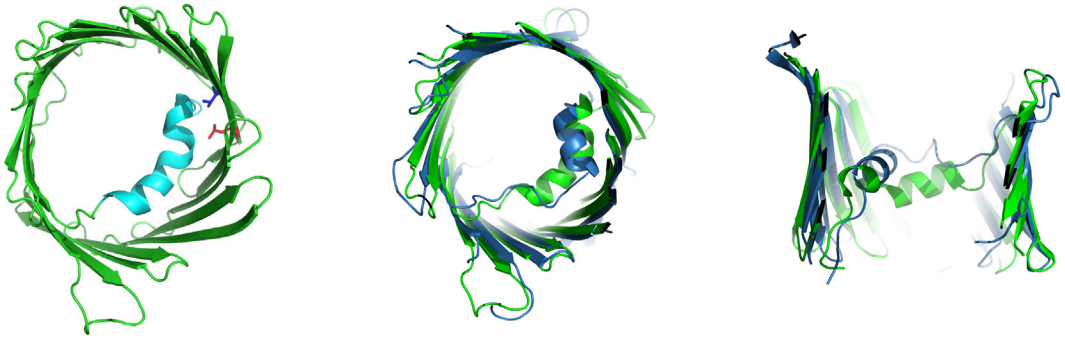

Fig. 3. Cartoon representations of VDAC according to the x-ray structure and an alternative NTS position corresponding to a near-native second free-energy minimum along the NTS dissociation pathway from the pore (wt2). (a) The x-ray structure (PDB ID 3EMN) of VDAC. Amino acids V143 and L150 are shown in blue and red stick representation, respectively. Residues 1–20 are highlighted in cyan color. (b) Top view of the overlay of the x-ray structure (PDB ID 3EMN) of VDAC (green) and the last snapshot of the simulation of wt2 (blue). (c) As panel b, but side view into the barrel. Simulation acronyms are explained in Table 1.

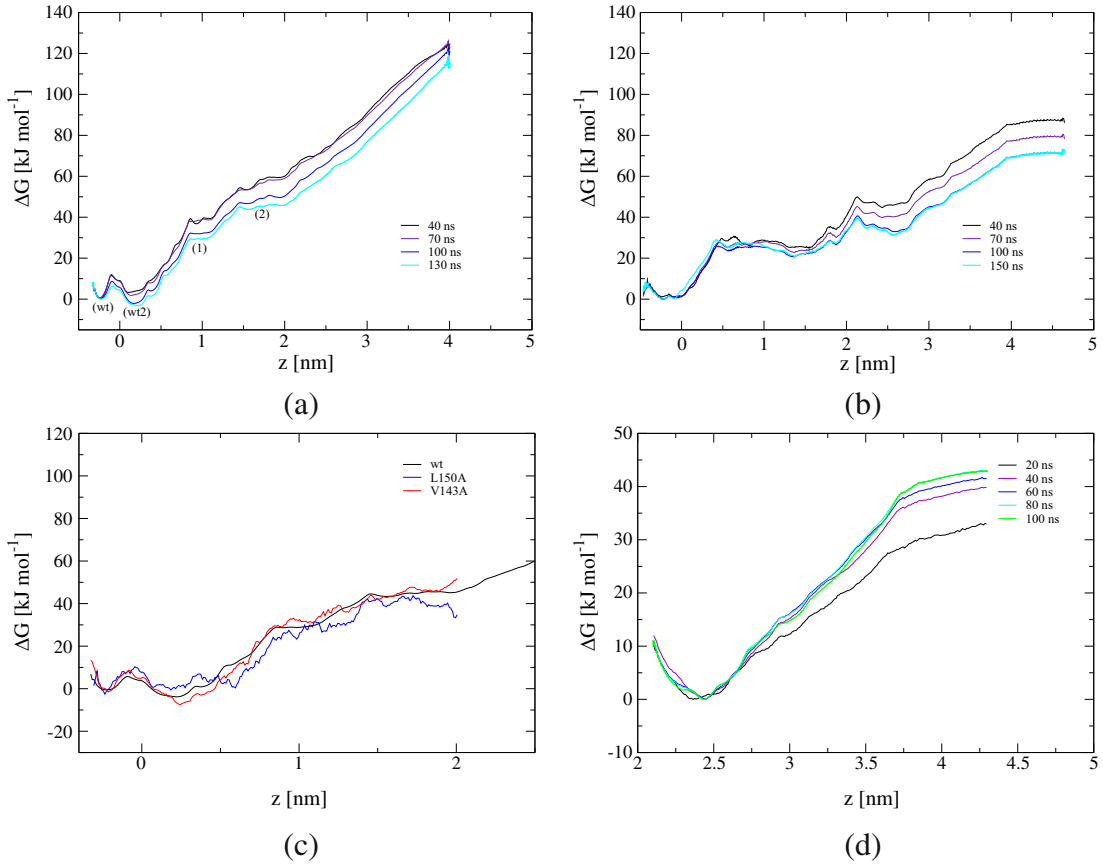

Fig. 4. Free-energy profiles for dissociation (a) of the NTS from the VDAC pore in the wild type system, PMF1, (b) of the NTS-derived peptide from the VDAC pore in the modified system involving a noncovalently bound NTS, PMF2, (c) of the NTS from the VDAC pore in mutants V143A and L150A compared to the VDAC wild type and (d) of the NTS-derived peptide from a pure membrane patch, M-PMF. The PMFs are shown along the *z*-coordinate of the distance vector between the com of the heavy atoms of the beta barrel (residues 27–283 for PMF1 and 25–283 for PMF2) or the membrane com for M-PMF and the com of the backbone atoms of NTS residues (residues 8–19 for PMF1 and the entire peptide for PMF2 and M-PMF). For PMF1, PMF2 and M-PMF, error bars from Monte Carlo bootstrapping are shown for the converged PMF. In panel a, label (wt) refers to the native NTS location as observed in the x-ray structure (PDB ID 3EMN) and label (wt2) refers to an NTS location in a second near-native free-energy minimum (Fig. 3). Labels 1 and 2 refer to plateau regions (1) and (2) in the PMF (Binding of the NTS to VDAC section) and here denote NTS locations at average *z*-values of 0.98 and 1.76 nm, respectively. Corresponding representative snapshots are provided in Fig. 5a and b, respectively. In panels a, b and d, the PMFs are depicted for increasing simulation lengths per window. For panel b, note that windows above $z = 4$ nm were only simulated for 40 ns. For panel c, the mutant PMFs are obtained from reweighting based on the wild type PMF. All PMFs are anchored to zero in the first local minimum. Simulation acronyms are explained in Table 1.

PMF windows, involve A8–D186, T6–D78, A8–D78, N79–D9, S104–D9, T107–D9, N216–G11, and G272–K20 (the donor is reported first). In Fig. 2b and c, selected hydrogen bonds occurring more than 30% of the simulation time in plateau region (2) are depicted (A8 NH with D78 OD1 and OD2, N79 HD21 with D9 OD1, S104 HG with D9 OD2 and T107 HG1 with D9 OD2). The calculated protein–membrane interaction energy in both plateau regions is more favorable in comparison to the native position of the NTS due to the membrane-vicinal location of the NTS. Considering, for simplicity, only the windows pertaining to the center of the two regions (on average 0.98 and 1.76 nm above the barrel com), protein–membrane Van der Waals interaction energies are increased in magnitude by 0.8% and 2.7% and electrostatic interaction energies by 6.4% and 13.3%, respectively.

(C) A steep rise for the dissociation of the N-terminal fragment from the membrane. No plateau is observed for the in-solvent location because an increased distance along the membrane normal implies increased tension on the first (N-terminal) strand in the β-barrel which is highly unfavorable.

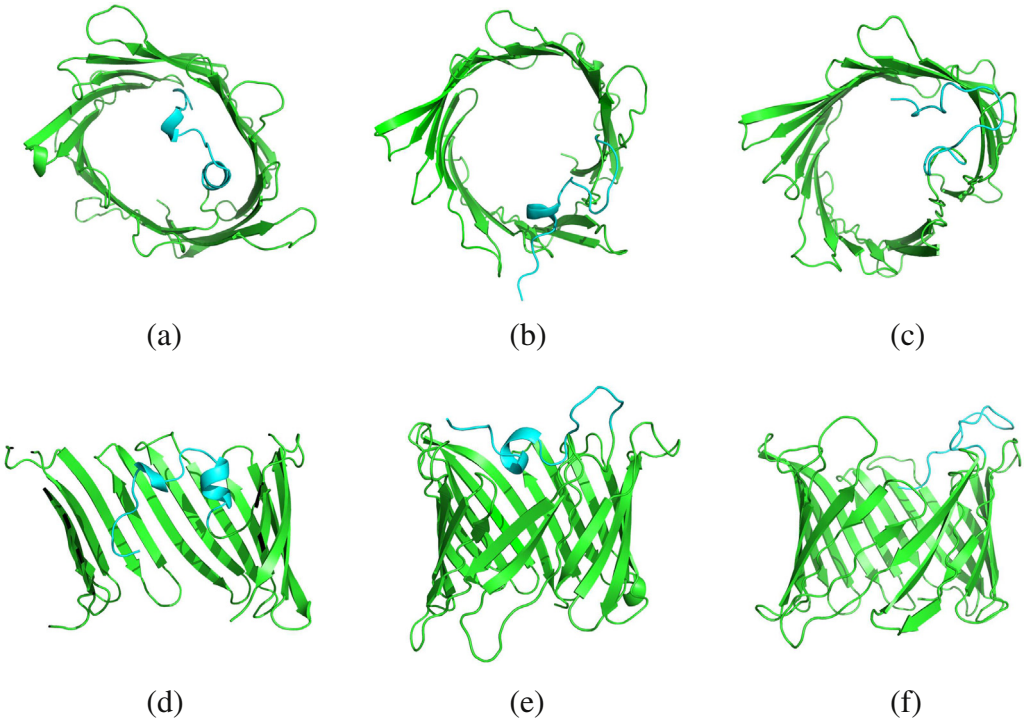

Fig. 5. Cartoon representations of VDAC. Residues 1–20 are highlighted in cyan color. (a) Last snapshot of the PMF window sampling an average distance of the NTS com of 0.98 nm above the barrel com. (b) Last snapshot of the PMF window sampling an average distance of the NTS com of 1.76 nm above the barrel com. (c) Last snapshot of the PMF window sampling an average distance of the NTS com of 2.24 nm above the barrel com. (d–f) Side view of the structures depicted in panels a–c, respectively.

The latter problem is circumvented in the case of the noncovalently bound NTS present as a 14-residue peptide (Fig. 4b). The corresponding free-energy profile also shows minima slightly (−0.23 and −0.09 nm) below the barrel com (separated by a negligible free-energy barrier of less than k_BT at room temperature), followed by a relatively flattened out region at distances of 0.57–1.09 nm and another relatively constant free-energy region at distances of $z = 2.3 - 2.7$ nm. The in-solvent position of the peptide is characterized by flattening of the PMF, starting around 4 nm from the barrel com. Thus, the basic features of PMF1 and PMF2 are very similar. In particular, the region at z values below 0 nm appears to be smeared out in PMF2, which indicates larger accessibility of different near-native NTS positions and may be interpreted as an analog of the occurrence of the wt2 minimum in PMF1 (although the latter occurs at a slightly larger z value of 0.17 nm). Consistent with the finding of larger accessibility of different near-native NTS positions in PMF2, a free simulation of the modified system with the noncovalently bound NTS-derived peptide (Vmod; Table 1) also shows increased motion of the peptide along the z-direction (Structural characteristics of VDAC in the wt2 position and comparison with Vmod section).

Along the dissociation pathway of the NTS in PMF1, the following structural changes occur (Fig. 6). (i) The helical structure content of the NTS varies in a range of 20%–40% while still in the barrel, decreases to around 10%–20% in the vicinity of the membrane surface and decreases significantly (<10%) once the solvent moiety is reached, consistent with previous circular dichroism and NMR studies [15] of the VDAC NTS in buffer, detergent micelles and lipid bilayer membranes. (ii) The orientation of the NTS changes only slightly within the pore. (iii) The shape of the barrel shows least ellipticity when the NTS is bound in the native position (similar *a*, *b*), reaches a maximum in ellipticity when the NTS is close to the barrel com and stays modestly elliptic for the remainder of the dissociation pathway, that is, slight deformation of the barrel shape occurs. Barrel shape variation appears to be more defined when unbinding of the NTS takes place, as indicated by the pronounced maxima in the ellipse orientation for large values of the reaction coordinate (Fig. S4). (iv) The backbone atom-positional rmsd from the energy-minimized x-

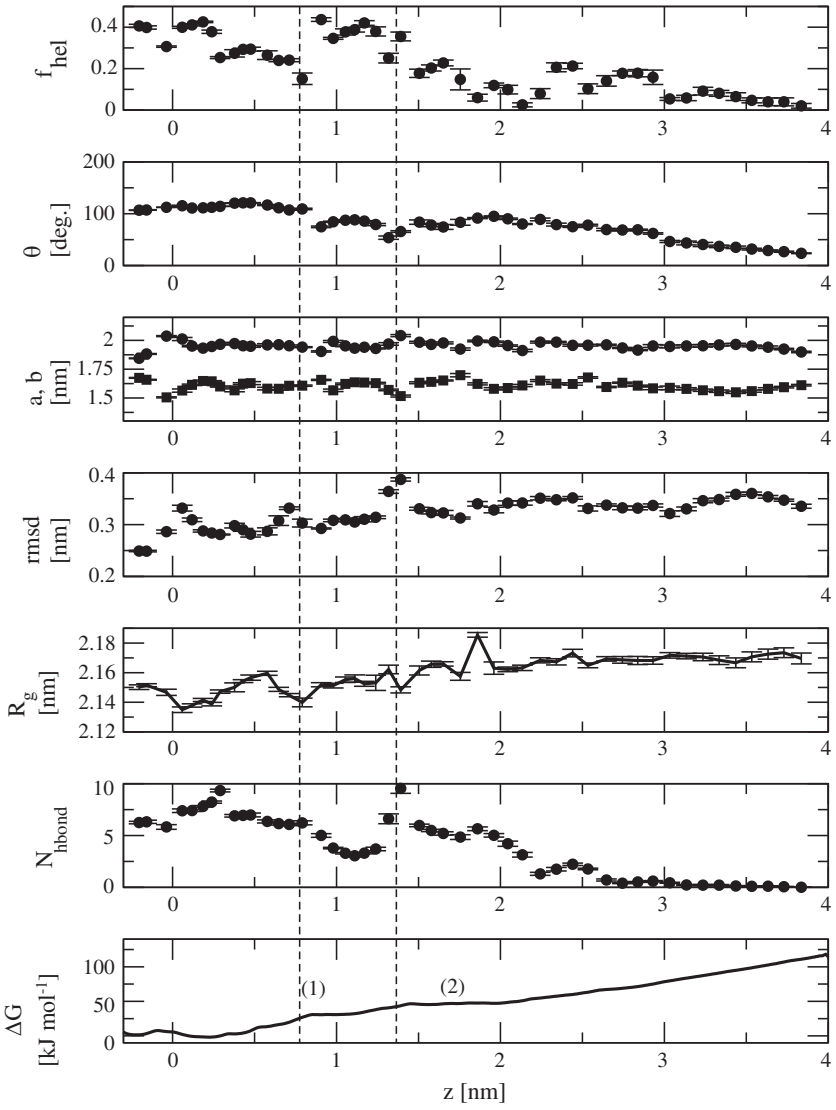

Fig. 6. Average helical content (f_{hel}) in the first 20 N-terminal residues, angle (θ) between the *z*-axis and the vector connecting C_α atoms of residues 9 and 18, semi-major (*a*) and semi-minor (*b*) ellipse axes, rmsd of barrel (residues 27–283) backbone atoms with respect to the energy-minimized x-ray structure (PDB ID 3EMN), radius of gyration (R_g) of the barrel (residues 27–283) backbone and number of hydrogen bonds (N_{hbond}) between the barrel (residues 27–283) and the first 20 N-terminal residues during the simulations of the 48 PMF windows for PMF1. The *x*-axis of the plots denotes the sampled average reaction coordinate in the respective PMF window. Errors from block averaging are indicated as vertical bars. The dashed vertical lines are a guide for the eye to identify the onset of plateau regions in the PMF. Labels 1 and 2 refer to plateau regions (1) and (2) in the PMF (Binding of the NTS to VDAC section) and here denote NTS locations at average *z*-values of 0.98 and 1.76 nm, respectively. Corresponding representative snapshots are provided in Fig. 5a and b, respectively. Simulation acronyms are explained in Table 1.

ray structure (PDB ID 3EMN) is consistent with the observed changes in *a* and *b*. It shows a peak close to the barrel com (rmsd 0.33 nm) along with further small peaks coinciding with corresponding changes in *a* and *b*. The rmsd maximum appears shortly before the onset of plateau region (2) in the PMF at $z = 1.4$ nm with an rmsd of 0.39 nm. For comparison, the minimum rmsd (corresponding to the wt position) is 0.25 nm, that is, the maximum barrel backbone atom-positional variation during NTS dissociation amounts to 56%. (v) Barrel shape change is also reflected in the radius of gyration R_g of barrel backbone atoms which is 2.15 nm in the wt position, reaches a minimum (2.13 nm) slightly below the wt2 position at $z = 0.06$ nm and a maximum ($R_g = 2.19$ nm at $z = 1.86$ nm) in plateau region (2). Beyond $z = 2$ nm, the radius of gyration is again smaller, but still on average 0.9% larger than in the wt NTS position. (vi) Hydrogen bond interactions between the NTS and the remainder of the protein only decrease to an essentially vanishing amount once the membrane surface region is left.

The dissociation pathway of the NTS in PMF1 is accompanied by the following energetic changes (Fig. 7). (i) Interactions with water are present throughout, become very favorable (local minima) in the two plateau regions (1) and (2) and become increasingly favorable with further dissociation into the solvent. Thus, the two plateau regions appear to be characterized by very favorable NTS hydration. Interestingly, a locally maximal (i.e., more unfavorable) electrostatic interaction energy between the NTS and water at 2.2 nm (i.e., just after plateau region (2)) is correlated with a locally minimal (i.e., more favorable) Van der Waals interaction energy between the NTS and water. This location of the

Table 1. Overview of the performed simulations

Simulation acronym	Protein	Simulation	Biomolecule net charge	Simulation time
wt	VDAC wt	Free	3 *e*	80 ns
wt2	VDAC wt, alt. pos.	Free	3 *e*	80 ns
V143A	VDAC V143A	Free	3 *e*	80 ns
L150A	VDAC L150A	Free	3 *e*	80 ns
PMF1	VDAC wt	PMF, HRE	3 *e*	120 ns per window
Vmod	VDAC mod.	Free	3 *e*	120 ns
PMF2	VDAC mod.	PMF, peptide, conf. Rest.	3 *e* (peptide 1 *e*)	40–150 n per window
M-NTS(1–4)	NTS	Free	1 *e*	400 ns
M-PMF	NTS	PMF, peptide, conf. Rest.	1 *e*	100 ns per window

Wild type (wt) and mutant (V143A, L150A) forms of the VDAC molecule, the former also with an alternative position of the NTS in the pore lumen (VDAC wt, alt. pos.) were simulated. PMF calculations of NTS dissociation were done for the wild type VDAC with a Hamiltonian replica exchange sampling scheme (HRE), for a modified VDAC molecule (VDAC mod.) involving a noncovalently bound 14-residue peptide derived from the VDAC NTS and for the peptide from a pure membrane patch. Biomolecule-associated net charge for these systems is indicated. Simulation acronyms and specifics of simulation approach and time are also reported.

NTS coincides with most favorable NTS–membrane interactions. A representative snapshot is shown in Fig. 5c and f. The NTS lies further outside the pore in great vicinity to the membrane headgroup region. It appears that the orientation of the water molecules near the membrane headgroup region (solvation of a plenitude of net charges, namely the positively charged choline and negatively charged phosphate groups) is electrostatically unfavorable for NTS hydration. (ii) Interactions with the rest of the protein (residues 21–283) approximately monotonously decrease in magnitude during the dissociation. The electrostatic and Van der Waals components present local plateau regions of relatively low magnitude in PMF plateau regions (1) and (2), respectively. In other words, regions (1) and (2) show constant and more unfavorable NTS–protein electrostatic and Van der Waals interactions, respectively, than the surroundings. (iii) Interactions with the membrane only appear noticeable in plateau region (2) of the PMF, when the NTS has reached the top of the barrel. Both the electrostatic and Van der Waals components are especially favorable (local minimum) at 2.2 nm. Above this distance, their magnitude decreases due to increasing membrane–NTS distance. In summary, considering energetic features, regions (1) and (2) of the PMF correspond to relatively favorable NTS hydration and unfavorable NTS–protein interactions. The onset of the PMF rise after region (2) corresponds to extremely favorable NTS–membrane interactions and NTS–water Van der Waals interactions, whereas NTS–protein interactions and NTS–water electrostatic interactions are unfavorable. The latter continue to get more favorable only above distances of 2.5 nm.

Comparing the energetic features of the minima in the PMF corresponding to wt and wt2 (Fig. 7), we note that wt2 has slightly less favorable electrostatic and more favorable Van der Waals NTS–water interactions and slightly more favorable electrostatic NTS–protein interactions. The Van der Waals component of the latter and NTS–membrane interactions are essentially unaltered.

The free energy of releasing conformational restraints in the peptide is similar in the pore lumen and outside the pore opening near the membrane headgroup region, twice as high in water and almost vanishing at the pure membrane surface (Table 4 and Fig. S2). Except for the latter environment, this free energy is negative, indicating favorable transition from the helically restrained conformation to a more unfolded peptide state. At the membrane surface, however, the peptide is preferentially in the helical conformation. This is consistent with experimental findings [15]. The corrected NTS–pore binding free energies ΔG_{bnd} (Eq. (7)) are reported in Table 4. Pulling the NTS-derived peptide from the pore lumen into the solvent is associated with a (reversible) work of 74.3 kJ mol^{-1}. This work is higher in the case of the covalently attached NTS (83.8 kJ mol^{-1}) because the presence of the linking region impedes dissociation. Translocating the peptide from the pore lumen to the membrane surface requires considerably less work (34.5 kJ mol^{-1}). Depending on the precise definition of the unbound state, this value may be even lower, for example, using as unbound state the minima at z = 1.9 nm (which is already in the vicinity of the pore exit) or z = 2.6 nm would result in values of 27 or 31 kJ mol^{-1}, respectively, assuming the same ΔG_{con} contributions. This corresponds to relatively weak binding.

A comparison between PMF1 and the reweighted PMFs pertaining to mutants V143A and L150A (Fig. 4c) shows that the free-energy difference between the wt minimum and the plateau region (2) is essentially unaffected for V143A and only marginally decreased for L150A. The small order of magnitude of the change is in agreement with corresponding end point MM-PBSA binding free-energy calculations (positive binding free-energy change of around 2.4 or 6.9 kJ mol^{-1} in mutants V143A and L150A, respectively; Table S1).

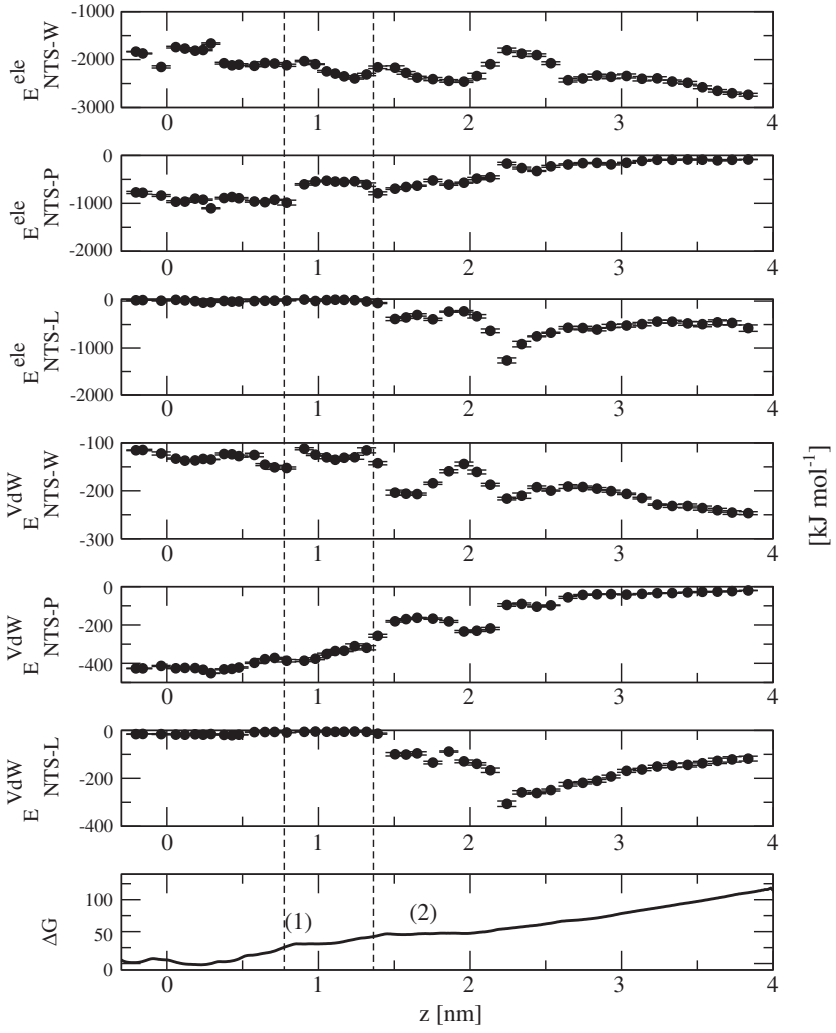

Fig. 7. Average electrostatic (superscript "ele") and Van der Waals (superscript "VdW") interaction energies between the NTS (residues 1–20) and water ("W"), the rest of the protein (residues 21–283; "P") and the lipid molecules ("L") during the simulations of the 48 PMF windows for PMF1. The employed interaction functions are the same as the ones used during the simulation (MD simulations section). The *x*-axis of the plots denotes the sampled average reaction coordinate in the respective PMF window. Errors from block averaging are indicated as vertical bars. The dashed vertical lines are a guide for the eye to identify the onset of plateau regions in the PMF. Labels 1 and 2 refer to plateau regions (1) and (2) in the PMF (Binding of the NTS to VDAC section) and here denote NTS locations at average *z*-values of 0.98 and 1.76 nm, respectively. Corresponding representative snapshots are provided in Fig. 5a and b, respectively. Simulation acronyms are explained in Table 1.

Experimental data suggest that both mutations facilitate NTS dissociation from the pore. For example, the NMR structure of VDAC (F. Hagn, personal communication, 2016) shows important interactions between the V143 and L150 side chains and the NTS. Moreover, refolding experiments give reduced yields for the mutants, which indicates that V143 and L150 are involved in hydrophobic NTS–barrel interactions that are important for adopting a stable tertiary structure.

Structural characteristics of VDAC in the wt2 position and comparison with Vmod

During the 80-ns production simulation wt2, the NTS adopts a stable position (Fig. 1; see also Fig. 3b and c for a representative snapshot). Per definition, the *z*-coordinate of the distance between barrel com and NTS com is offset by about 0.4 nm with respect to wt. Although wt and wt2 are separated by a low free-energy barrier (Binding of the NTS to VDAC section), no transitions between the two NTS positions were observed on the simulated timescale. The extent of helical secondary structure in the first 20 N-terminal residues is similar in simulations wt and wt2, but residues A8–G21 show much less helical structure in simulation wt2 (fraction of helical residues 54% *versus* 39%; Table 2). The system with the noncovalently bound NTS-derived peptide, Vmod, has almost unaltered helical content in the concerned residues (A8–G21), 50% in comparison to 54% in simulation wt.

The orientation of the NTS differs in the wt2 system in that it is somewhat more aligned with the membrane normal (mean angles θ formed with the membrane normal of 103.9, 101.6 and 102.3 deg. in simulations wt, V143A and L150A, respectively, compared to 119.5 deg. in simulation wt2). The fluctuation in the distance between barrel com and NTS com is somewhat larger in simulation wt2 than in simulations of the other systems (standard deviations of 0.05, 0.04 and 0.05 nm in simulations wt, V143A and L150, respectively, compared to 0.06 nm in simulation wt2). This might be due to the

Table 2. Fraction of residues with helical structure among (a) residues 1–20 or (b) residues A8–G21 in systems wt, wt2, V143A and L150A or, equivalently, A5–G18 in systems Vmod and M-NTS1–M-NTS4

	wt	wt2	V143A	L150A	Vmod	M-NTS1	M-NTS2	M-NTS3	M-NTS4
(a)	0.38 ± 0.007	0.42 ± 0.005	0.43 ± 0.010	0.43 ± 0.007	–	–	–	–	–
(b)	0.54 ± 0.007	0.39 ± 0.017	0.52 ± 0.009	0.52 ± 0.007	0.50 ± 0.007	0.47 ± 0.004	0.09 ± 0.04	0.45 ± 0.045	0.30 ± 0.027

Errors are from block averaging. Simulation acronyms are explained in Table 1.

changed NTS orientation in simulation wt2 because, intuitively, stronger alignment with the membrane normal as indicated by the angle θ (Fig. 1) provides more space in the surrounding pore lumen. Note that the distance in V143A is shifted toward that observed in simulation wt2. The distribution of φ (Fig. S3) is more smeared out in the wt2 system than in the other systems, indicating a slightly less defined barrel shape variation in simulation wt2. The enhanced shape flexibility could also contribute to the somewhat larger fluctuations in the position of the NTS in simulation wt2 (Fig. 1).

The very stable hydrogen bond between the backbones of A2 and H122 present in simulation wt persists in simulation wt2 with an even larger occurrence (97.3% *versus* 91.9%; Table 3). Similarly to mutant L150A, wt2 also has a very stable hydrogen bond between the side chains of Y7 and N168.

Comparing the structural features of the mutants (Structural characteristics of VDAC wild type and mutants V143A and L150A section) to wt2, V143A and wt2 have similarities concerning the location of the NTS which appears slightly further away from the barrel com (as is the case for wt2) (Fig. 1) and concerning the barrel shape which is somewhat similar to wt2 considering the less pronounced maxima in the φ distribution. In contrast, in mutant L150, it is the hydrogen bond pattern that is somewhat more similar to wt2. This might facilitate transition of the NTS to an alternative position akin to that in simulation wt2. However, although wt2 is further along the dissociation pathway reaction coordinate than wt, we emphasize that the NTS binding free energy to the wt2 state is not less negative than to wt (Binding of the NTS to VDAC section).

Table 3. Hydrogen bonds between the beta barrel (residues 27–283) and residues 1–20 occurring more than 50% of the simulation time in systems wt, wt2, V143A and L150A

Donor	Acceptor	Occ. (%)
wt		
K236 NZ	F18 O	63.7
N124 ND2	P4 O	77.1
H122 N	A2 O	91.9
A14 N	Q179 OE1	74.7
wt2		
H122 N	A2 O	97.3
Y7 OH	N168 OD1	93.5
V143A		
N124 ND2	P4 O	92.5
H122 N	A2 O	55.5
A14 N	Q179 OE1	66.1
L150A		
N168 ND2	Y7 OH	54.6
N124 ND2	P4 O	52.0
H122 N	A2 O	63.3

Simulation acronyms are explained in Table 1.

To summarize, differences between wt and wt2 concern fluctuations in the position of the NTS, barrel shape characteristics, secondary structure stability of the NTS and hydrogen bond interactions between the NTS and the barrel moiety. Note that the simulation involving the VDAC barrel and a noncovalently bound NTS-derived peptide (Vmod; Table 1) displays a similar NTS–barrel com–com distance as observed in the wt system, but the z-component of the distance vector is clearly more shifted toward wt2 and the NTS orientation is congruent with that in wt2 (Fig. 1). This is a confirmation of alternative NTS positions and orientations close to the native (x-ray structure-like) wt state. In particular, simulation Vmod starts initially with the NTS positioned at $z = -0.4$ nm, but the NTS migrates quickly upward and stays from about 1.5 to 6 ns around $z = -0.2$ nm (similar to wt) before jumping to values around $z = 0$. After around 37 ns, the NTS moves slightly downward again, leading to an overall probability distribution of z that peaks at −0.05 nm, to be compared with −0.28 nm for wt and 0.19 nm for wt2. The widths of the distributions, estimated by the full width at half maximum, are 0.11, 0.13 and 0.13 nm in the wt, wt2 and Vmod simulations, again indicating similarity, here in terms of NTS com positional flexibility, of the wt2 state and the noncovalently bound NTS. The positional flexibility of the Vmod NTS below z = 0 is in agreement with the shape of the PMF in this regime (Fig. 4b).

Binding of the NTS to the membrane

NMR measurements on a system containing nanodiscs and the VDAC NTS showed CSPs indicative of VDAC–nanodisc binding (Fig. 8a–c),

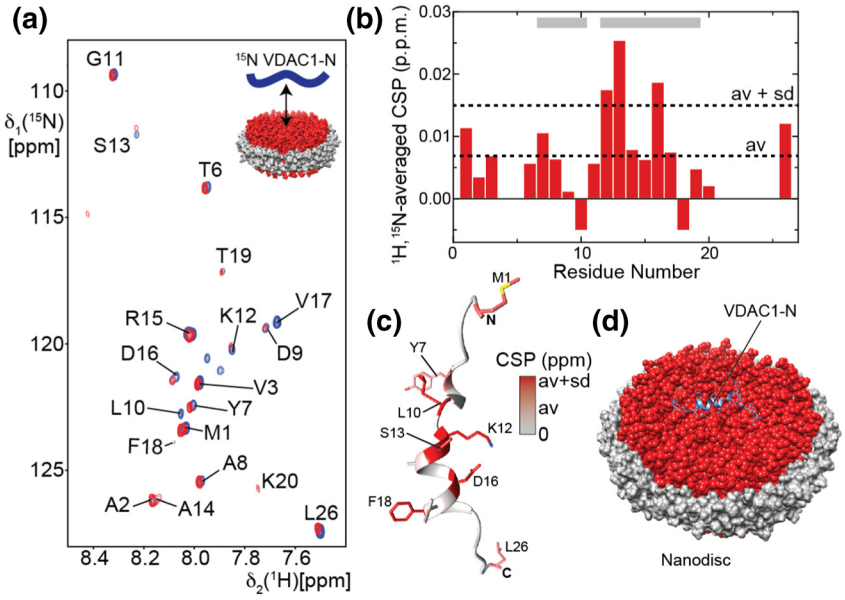

Fig. 8. Interaction of the VDAC NTS and a lipid surface as probed by NMR. (a) Two-dimensional [^{15}N;^{1}H]-TROSY spectra of ^{15}N-labeled VDAC NTS in buffer (blue) or in the presence of a 5-fold excess of phospholipid nanodiscs assembled with MSP1D1 protein and *E. coli* polar lipids (red), mimicking the lipid composition of mitochondria. Assigned resonances in the VDAC NTS are labeled. (b) ^{15}N,^{1}H-averaged CSPs of nanodisc binding to the VDAC NTS. Broken lines indicate the average CSP (av) or the average plus 1 standard deviation (av+sd). Negative bars indicate disappearing resonances within the VDAC NTS upon the addition of nanodiscs. The α-helical secondary structure content of the VDAC NTS taken from the x-ray structure (PDB ID 3EMN) [11] is indicated by gray boxes. (c) CSP values in panel b mapped onto the structure of the VDAC NTS and color-coded from gray to red, as indicated by the legend (av: average CSP; av+sd: average plus 1 standard deviation). Disappearing resonances are also colored in red, and affected amino acid residues are labeled. (d) Model of the VDAC NTS nanodisc interaction obtained by manual docking in Chimera [28].

with a mean CSP of 0.0075 p.p.m. Residues K12, S13 and D16 have particularly high CSPs, exceeding the mean CSP plus 1 standard deviation, which is also a strong evidence of nanodisc binding. A model of the NTS docked to the membrane surface is shown in Fig. 8d, where hydrophobic side chains are oriented toward the membrane. The performed one-step titration experiments cannot give reliable estimates of the peptide-nanodisc binding free energy. The binding free energy from the PMF simulation (M-PMF; Fig. 4d and Table 4) is −39.0 kJ mol^{-1}, which corresponds to a K_d value in the rather low μM range, consistent with the observation of fast (changes in peak position) and intermediate (peak broadening) exchange in the NMR spectra (Fig. 8a).

The free membrane-binding simulations M-NTS1–M-NTS4 show continuous (M-NTS1, M-NTS3) or recurring (M-NTS2, M-NTS4) presence of helical structure in the membrane-bound peptide (Fig. S5). The involved residues (mainly K12–F18) are

Table 4. Quantities involved in calculation of the NTS–pore or NTS–membrane binding free energy ΔG_{bnd} (Eq. (7))

Simulation	ΔG_{raw} (kJ mol^{-1})	ΔG_{con}(bound) (kJ mol^{-1})	ΔG_{con}(unbound) (kJ mol^{-1})	ΔG_{std} (kJ mol^{-1})	ΔG_{bnd} (kJ mol^{-1})
PMF1[a]	−83.8 ± 0.1	–	–	–	−83.8 ± 0.1
PMF2[b,c]	−72.8 ± 0.3	−4.1 ± 0.1	−9.4 ± 0.1	−6.8	−74.3 ± 0.5
PMF2[b,d,e]	−35.1 ± 0.2	−4.1 ± 0.1	−4.7 ± 0.1	–	−34.5 ± 0.4
M-PMF[a]	−44.4 ± 0.2	1.1 ± 0.1	−9.4 ± 0.1	−5.1	−39.0 ± 0.4

The "raw" binding-free energy value obtained from the PMF ΔG_{raw} (Eq. (8)), the free energies of releasing conformational restraints ΔG_{con} (Eq. (6)) in the bound and unbound state and the standard-state correction ΔG_{std} (Eq. (9)) are reported for simulations PMF1, PMF2 and M-PMF. Errors are from Monte Carlo bootstrapping. Simulation acronyms are explained in Table 1.

[a] The unbound state was chosen as described in the Free-energy calculations section.
[b] The bound state was chosen as the first local minimum (z = − 0.22 nm).
[c] The unbound state refers to the solvent (z = 4.1 − 4.6 nm).
[d] The unbound state refers to the vicinity of the membrane headgroup region (z = 2.3 − 2.7 nm).
[e] The reported value for ΔG_{bnd} refers to an unbound state with an accessible volume corresponding to the membrane patch size employed during the simulation.

congruent with helical structure present in the x-ray structure. The rmsf values of C_α atoms in the bound peptide are similar in simulations M-NTS1, M-NTS3 and M-NTS4 (around 0.1–0.25 nm) and somewhat elevated in simulation M-NTS2 (up to 0.5 nm; Fig. S6), with the latter being consistent with the relatively small amount of secondary structure in simulation M-NTS2 (Fig. S5). Conformational cluster analysis of the pool of configurations obtained from simulations M-NTS1–M-NTS4 shows that the first three clusters, encompassing mostly simulations M-NTS1, M-NTS3 and M-NTS4, contain a high amount of helical secondary structure (fraction 0.40–0.46). Simulation M-NTS2 mostly samples configurations from the more unstructured fourth cluster (Fig. S7).

In the following, clustering with respect to peptide position on the membrane assumes that the peptide is bound on the membrane side with negative *z*-axis, with $z = 0$ denoting the membrane com. Clustering in terms of residue alignment in comparison to the *z*-axis shows similarities between simulations M-NTS1 and M-NTS4, which indicates that the manual positioning of the peptide in the beginning of the former simulation did not lead to a spurious bias but yields peptide orientations akin to those found in a simulation with free binding (Fig. S8). Note that an angle >90 deg. in Fig. S8 indicates that the side chain points toward the membrane, the opposite being the case for an angle <90 deg. Thus, clusters 1–3 consistently show that the side chains of residues K12, F18 and K20 point toward the membrane and of residues D9, S13 and D16 point toward the solvent. The helical content of the first two clusters is close to 40%.

Clustering in terms of residue height above the membrane com shows that clusters 1–3 are similar with respect to the terminal residues, but differ significantly toward the middle of the peptide (Fig. S9). In particular, the coms of K12, S13 and V17 are more solvent vicinal in cluster 2, whereas they are more membrane vicinal in clusters 1 and 3. Cluster 3 presents close membrane attachment in the region L10–A14, and cluster 1 presents solvent vicinity of the region A14–D16. Thus, the sampled peptide configurations are rather diverse concerning the per-residue distance from the membrane com (range of −3 to −2 nm). Overall, the peptide com of the configurations in simulations M-NTS1–4 samples a similar *z*-coordinate distance range from the membrane com (Fig. S10). This range energetically exceeds the minimum-free energy position of M-PMF ($z = 2.45$ nm from the membrane com; Fig. 4) by more than k_BT, which may be due to the helical restraints applied in the PMF calculation. The central member structures of the largest cluster in each of the three performed clustering procedures are shown in Fig. S11. Common features are the solvent exposure of the C-terminus and the D16 side chain, the approximately membrane-parallel alignment of the D9 side chain, the approximately membrane-parallel or membrane-oriented location of the K12 side chain and the approximately membrane-parallel or in-solvent orientation of the S13 side chain.

Conclusion

In this work, we investigated the dissociation of the NTS of VDAC from the pore into the solvent (corresponding to the cytoplasmic environment of VDAC), as well as the binding to a membrane. For the former, two systems were considered, either the wild type system or a modified system with a noncovalently bound NTS-derived peptide. Moreover, two VDAC variants containing mutations in the direct interaction site of the NTS and the barrel were investigated.

Computational studies involving the NTS of VDAC are complicated by the dependence of its secondary structure content on the environment. Adequate conformational sampling requires the use of enhanced sampling methods and/or conformational restraints along with successive estimation of the free energy of releasing the restraints. Using both strategies in the performed MD simulations, our main findings are as follows:

(1) The free energy required to translocate the VDAC NTS from the pore lumen into the solvent is on the order of 80 kJ mol^{-1}, rendering spontaneous NTS dissociation into the solvent very unlikely.
(2) Simulations of dissociation of the noncovalently bound NTS from the VDAC pore toward the membrane surface at a distance of $z = 2.3 - 2.7$ nm indicate a free-energy change of 35 kJ mol^{-1}, which translates to $K_d \approx 0.8$ μM. Depending on the precise definition of the unbound state, the binding may be even weaker; for example, using as unbound state the minima at $z = 1.9$ nm (which is already in the vicinity of the pore opening) or $z = 2.6$ nm would result in values of 27 or 31 kJ mol^{-1}, respectively, that is, K_d values of 20 or 4 μM, respectively. This corresponds to rather weak binding. Simulations including the covalent link between the NTS and the barrel predict a higher free-energy change.
(3) NTS dissociation from the native location in the wild type VDAC to a position at the pore opening is associated with a large positive free-energy change of about 45 kJ mol^{-1}. Thus, spontaneous NTS dissociation from the pore appears impossible. Future work will investigate whether the presence of additional proteins vicinal to VDAC and resident in the membrane and/or in the cytoplasmic neighborhood may facilitate NTS dissociation.

Favorable NTS binding to another protein could possibly compensate for the work required to translocate the NTS from the native in-pore position toward the membrane surface.

(4) Besides the free-energy minimum pertaining to the native NTS position as present in the x-ray structure (wt), the dissociation pathway shows a second minimum shifted by about 0.4 nm toward the pore opening (wt2). This minimum is slightly more thermodynamically stable but was not accessed during the simulations starting from the x-ray structure. The separating barrier height is only a few $k_B T$. In analogy to this minimum in the VDAC system, a modified system (Vmod) featuring a noncovalently bound NTS-derived peptide shows a smeared out near-native free-energy landscape, that is, possible alternative NTS positions within the barrel. A less defined position of the NTS in the pore appears compatible with an experimental NMR bundle of VDAC structure (F. Hagn, personal communication, 2016). Interestingly, NTS orientation in the Vmod and wt2 systems is similar and different from that in system wt.

(5) Slight changes in pore shape occur during the dissociation, as evident from barrel elliptic shape parameters, barrel backbone atom-positional rmsd from the x-ray structure and barrel radius of gyration. Thus, one may speculate that rigidification of the VDAC pore might impair NTS dissociation.

(6) While the NTS shows helical structure in the pore lumen and in the vicinity of the membrane surface, it is unstructured in solution.

(7) The description of the effect of the point mutants V143A and L150A is only compatible with experimental findings of loser NTS–pore binding in case of L150A. According to our results from the reweighted wild type PMF, mutation V143A leaves the binding free energy of the NTS essentially unaltered.

Our study provides important insight into the thermodynamic, dynamic and structural features of VDAC.

Materials and Methods

MD simulations

All simulations were performed with the gromacs 5.1.2 engine [29,30]. Some simulations employed gromacs combined with the PLUMED 2.2.2 package [31]. Simulation pre- and post-processing tasks were performed with the gromacs 4.6.5 or 5.1.2 packages [29,30] or the gromos++ program package [32]. For all simulations, the GROMOS 54A7 force-field version [33] was used.

We simulated five different systems, each involving a solvated POPC bilayer and the following proteins: (i) the VDAC molecule (based on PDB ID 3EMN [11]); (ii) mutants L150A and V143A of the VDAC molecule; (iii) the VDAC molecule with the NTS at a non-native position within the pore lumen; (iv) a modified VDAC molecule with the first 24 N-terminal residues removed, that is, starting with G25, in complex with the isolated NTS present as a short peptide comprising residues A8–G21 (the choice of residues was motivated by an NMR study of the isolated NTS; F. Hagn, personal communication, 2016); and (v) the isolated NTS present as a short peptide comprising residues A8–G21.

All simulations were performed under periodic boundary conditions at constant temperature (300 K) and pressure (1 bar). Unless specified otherwise, thermostatting and barostatting were performed using the weak-coupling scheme [34], with coupling times of 0.1 and 1 ps, respectively, as well as an isothermal compressibility appropriate for water ($4.5 \cdot 10^{-5}$ bar^{-1}) for the barostat. Protein, membrane and solvent (water and, if present, ions) components were separately coupled to the temperature bath. The barostatting was applied semi-isotropically in simulations involving membranes. Otherwise, the simulation box was scaled isotropically. The LINCS algorithm [35] was used to constrain all bond lengths to their reference values. The equations of motion were integrated according to the leap-frog algorithm [36], with a step size of 0.002 ps. A buffered (Verlet) pair list was created based on a maximum allowed error for pair interactions per particle of 0.005 kJ mol^{-1} ps^{-1}. It was updated every five time steps. Van der Waals interactions were modeled with the Lennard–Jones potential, truncated at a distance of 1.4 nm. Electrostatic interactions were computed using cutoff truncation at 1.4 nm in combination with a reaction-field correction [37] based on a relative dielectric permittivity of 61, as appropriate [38] for the SPC water model. A lattice-sum electrostatics scheme was refrained from to minimize periodicity artifacts. Counterions were not included in simulations to avoid spurious ion–membrane interactions due to possibly inappropriate force-field parameters [39]. An overview of the performed simulations is provided in Table 1.

Unless mentioned otherwise, coordinates and energies were written to file every 4 ps. Simulation times (exempt of the thermalizing equilibration period) are reported in Table 1.

Setup of simulations

VDAC simulations were based on the x-ray structure with PDB ID 3EMN [11]. This structure misses side chain atoms in K161 which were

modeled based on alignment of the barrel with the NMR structure (PDB ID 2K4T) [12]. An equilibrated hydrated POPC bilayer consisting of 64 lipids per layer was downloaded from the Automated Topology Builder and Repository [40]. It was duplicated along the *x*- and *y*-directions, and water molecules were removed. Using the gromacs editconf and genbox tools [29,30], the protein and membrane components were combined into a single system. Here, the Van der Waals radii were artificially decreased to 0.08 nm to avoid large voids between the protein and the lipid molecules. The resulting system was visually inspected with the program vmd [41], version 1.9.1. Lipid molecules that were still present within the barrel lumen were removed manually. Then, harmonic position restraints were applied to all protein atoms and the system was energy-minimized to relax the lipid molecules surrounding the protein. The system was then solvated with the SPC water model [42], water molecules that were placed within the membrane were removed manually, another energy minimization with harmonically positionally restrained protein atoms was done and five successive equilibration steps of 20 ps length were performed. The first step served to relax the pressure along the *z*-direction and involved a very tight thermostatting (weak coupling [34] with a constant of 0.02 ps) to 100 K for the protein and membrane and 300 K for the water molecules, as well as barostatting to 1 bar along the *z*-direction (weak coupling [34] with a constant of 1 ps). Harmonic position restraints on all protein and lipid atoms with a force constant of 10,000 kJ mol^{-1} nm^{-2} along each spatial dimension were applied. The next two equilibration steps were exempt of barostatting but thermostatted to 200 and 250 K, respectively, with reduced position restraint force constants of 5000 and 2500 kJ mol^{-1} nm^{-2}, respectively. In the fourth and fifth steps, which were conducted at 300 K, semi-isotropic barostatting with a weak-coupling constant of 5 and 1 ps, respectively, along all directions was introduced and the position restraints were removed. Finally, a sixth equilibration step with settings equivalent to the previous step was performed for a length of 10 ns. The resulting system had box dimensions of about 9.4 × 9.4 × 9.6 nm^3. Its simulation is denoted "wt" (Table 1).

Initial coordinates for the windows pertaining to VDAC PMF calculations were obtained by slowly (rate 0.00015 nm ps^{-1}) pulling apart the center of mass (com) of the barrel (defined as the heavy atoms of residues 27–283) and the com of the heavy atoms of residues 8–19, as well as the com of the barrel and the com of the heavy atoms of residues 1–5 during a period of 20 ns. In a further 10-ns simulation starting from the final coordinates of the previous simulation, the com of residues 1–5 was pulled even further into the solvent (same pulling rate as above). In another 10-ns simulation starting again from the final coordinates of the previous simulation, the com of residues 8–19 was slowly pulled back toward the barrel (same pulling rate as above). This was done to obtain structures where the NTS is positioned at various com–com distances from the barrel, with the residues close to the N-terminus (residues 1–5) still immersed in solvent. Thus, one avoids obtaining structures where the N-terminal residues are bound strongly to the membrane headgroup atoms. During all these simulations, coordinates were written to file every 2 ps. From the pool of coordinates, structures with barrel-NTS com–com *z*-coordinate distances of −0.20, −0.12, −0.05, 0.02, 0.10, 0.18, 0.25, 0.32, 0.39, 0.46, 0.53, 0.60, 0.68, 0.76, 0.84, 0.91, 0.98, 1.06, 1.13, 1.20, 1.27, 1.34, 1.42, 1.50, 1.58, 1.66, 1.76, 1.86, …, 3.66, 3.76 and 3.86 nm were extracted. These distances were manually chosen to achieve sufficient overlap between the distance histograms in the corresponding PMF calculation (Free-energy calculations section).

The VDAC system was also simulated with an alternative position of the NTS (simulation wt2; Table 1). This alternative position corresponds to another near-native minimum in the PMF along the *z*-coordinate distance of barrel com and NTS com. Initial coordinates for simulation wt2 are the coordinates after 60 ns of an appropriate window of the PMF simulation. Furthermore, two point mutants of the VDAC system were simulated (V143A and L150A; Table 1). Initial coordinates of the mutants were obtained by removing side chain atoms from the equilibrated wild type VDAC system.

VDAC simulations involving the noncovalently bound NTS-derived 14-residue peptide were setup as follows: The first 24 residues of the last frame of simulation wt were removed, and a new terminus was created at G25. The VDAC protein was thus modified to only contain the barrel architecture. From an NMR study involving a (helical) peptide composed of residues 8–21 of the VDAC NTS (F. Hagn, personal communication, 2016), the peptide coordinates were then manually inserted into the barrel, in vicinity of the location of the respective residues in the original VDAC system. The system was energy-minimized to remove steric clashes between peptide and barrel residues, as well as peptide residues and water molecules. A 120-ns simulation of the resulting system, labeled "Vmod" (Table 1), was done to verify stability of the noncovalent peptide–barrel complex. Initial structures for the windows pertaining to PMF calculations were obtained by slowly (rate 0.0002 nm ps^{-1}) pulling apart the coms of the sets of heavy atoms of the two binding partners during a period of 20 ns and extracting structures with com–com *z*-coordinate distances of −0.31, −0.20, −0.11, 0.02, 0.12, 0.22, 0.33, 0.38, 0.45, 0.56, 0.67, 0.77, 0.88, 0.98, 1.08, 1.20, 1.31,

1.41, 1.52, 1.64, 1.74, 1.85, 1.94, 2.05, 2.11, 2.16, 2.26, 2.38, 2.49, 2.60, 2.73, 2.82, 2.94, 3.03, 3.14, 3.24, 3.36, 3.46, 3.56, 3.65, 3.70, 3.80, 3.90, 4.00, 4.10, 4.20, 4.30, 4.40 and 4.50 nm. These distances were manually chosen to achieve sufficient overlap between the distance histograms in the corresponding PMF calculation (Free-energy calculations section).

Finally, three systems containing the solvated 64 × 2 POPC bilayer and the above 14-residue NTS-derived peptide were created. In one system, the peptide was bound to the membrane in an orientation where the helix was approximately parallel to the membrane plane. The positioning was performed manually in a random rotation around the helix axis. In the other system, the peptide was put into the solvent phase, approximately 1 nm above the membrane headgroup area. The two systems contained 4965 and 4915 water molecules, respectively. The simulation of the former system is denoted M-NTS1. Three simulations of the latter system were conducted, differing in the initial velocities and denoted M-NTS2, M-NTS3 and M-NTS4. A third, larger system involving the equisized membrane patch, a solvated peptide and a solvent phase of 8557 water molecules was built to perform a PMF calculation of peptide–membrane binding. Initial structures for windows pertaining to a PMF calculation were obtained by pulling (rate 0.0024 nm ps^{-1}) together the coms of the sets of heavy atoms of the membrane and the peptide during a period of 1 ns and extracting structures with com–com *z*-coordinate distances of 4.2, 4.1, …, 2.3, 2.2 nm.

Free-energy calculations

Three PMFs were calculated for unbinding of the NTS in the wild type VDAC system, of the NTS-derived peptide in the modified VDAC system and of the NTS-derived peptide from the pure membrane patch, labeled PMF1, PMF2 and M-PMF, respectively (Table 1). PMF1 was calculated *via* sampling 48 windows of the covalently attached NTS with varying com–com *z*-coordinate distances as described in the Setup of simulations section. The coms pertaining to the barrel and the NTS were based on the heavy atoms of residues 27–283 and residues 8–19, respectively. Harmonic distance restraints were applied with a force constant of 1500 kJ mol^{-1} nm^{-2} along the *z*-axis. Sampling was performed with a Hamiltonian Replica Exchange (HRE) [43–45] scheme, where configuration exchanges between neighboring windows were attempted every 1000 time steps. Figure S1 provides a schematic representation of VDAC, the location of the barrel com and the *z*-axis.

PMF2 was calculated *via* sampling 49 windows of the NTS-derived peptide with varying com–com *z*-coordinate distances as described in the Setup of simulations section. The coms pertaining to the barrel and the NTS peptide were based on the heavy atoms of the two binding partners. Harmonic distance restraints were applied with a force constant of 1500 kJ mol^{-1} nm^{-2} along the *z*-axis. In addition, the φ and ψ backbone dihedral angles of residues L3–T12 of the peptide were restrained with a force constant of 300 kJ mol^{-1} rad^{-2} to values obtained as averages over a 160-ns simulation of the peptide in a system where it adopts a helical conformation (F. Hagn, personal communication, 2016). The first and last two residues were not restrained to alleviate movement of the peptide through the pore and because in an independent simulation, the two N-terminal residues were virtually never and the two C-terminal residues were not consistently in a helical conformation. Since the sampling task is reduced due to the conformational restraints, here the HRE scheme was not applied. The trick to apply restraints to reduce the sampling problem in binding free-energy calculations was suggested by Woo and Roux [46] in the context of protein–ligand binding and has recently also been used in protein–protein binding free-energy calculations [47,48]. Although conformational sampling in the simulation of the binding reaction is alleviated by conformational restraints, additional simulations have to be performed to estimate the free energy associated with releasing these restraints in the bound and unbound state. The determination of these free energies is often computationally intensive as well as non-trivial due to potential end point problems and multiple approaches have been suggested for their calculation [47,48].

M-PMF was calculated *via* sampling 21 windows of the isolated NTS, present as a 14-residue peptide, with varying com–com *z*-coordinate distances as described in the Setup of simulations section. The coms pertaining to the membrane and the peptide were based on all atoms of the membrane and all heavy atoms of the peptide, respectively. Harmonic distance restraints were applied with a force constant of 1500 kJ mol^{-1} nm^{-2} along the *z*-axis. In addition, the φ and ψ backbone dihedral angles of residues L3–T12 of the peptide were restrained as in the case of PMF2.

For all three PMFs, the sampled distance distributions were unbiased and converted into a free-energy profile *via* the weighted histogram analysis method (WHAM) [49–51]. Statistical errors along the PMF were calculated according to the Monte Carlo bootstrapping method implemented by Grossfield [51]. To interpret the obtained PMFs, for PMF2 and M-PMF, the free energy of releasing the conformational restraints on the dihedral angles τ_i, ΔG_{con}, has to be evaluated. In theory, one could do this with thermodynamic integration (TI) [52,53], where the

force constant of the dihedral angle restraints is made dependent on a coupling parameter λ, that is,

$$k(\lambda) = (\lambda-1)^2 K_0, \quad (1)$$

and thus, the λ-dependent part of the Hamiltonian and its λ-derivative are

$$H(\lambda) = \frac{1}{2} k(\lambda) \sum_i \left(\tau_i - \tau_{i,0}\right)^2 \quad (2)$$

and

$$\frac{\partial H}{\partial \lambda} = (\lambda-1) K_0 \sum_i \left(\tau_i - \tau_{i,0}\right)^2, \quad (3)$$

respectively. Here, $\tau_{i,0}$ denotes the target value for backbone dihedral angle τ_i and K_0 the restraining force constant in the PMF calculations. An advantage is that the quadratic-power dependence in Eq. (1) causes $\frac{\partial H}{\partial \lambda}$ to vanish for $\lambda = 1$ where, due to the absence of restraining potential in the sampling of peptide conformations ($k(\lambda = 1.0) = 0$), very large values of $(\tau_i - \tau_{i,0})^2$ are sampled due to the unfolded state of the peptide. Such a "hidden restraint" approach [54,55] was used recently in the context of protein–protein binding free-energy calculations with application of conformational restraints [48]. In practice, however, here this approach turned out difficult because at other λ-values close to unity ($\lambda > 0.85$), $\frac{\partial H}{\partial \lambda}$ in Eq. (3) started to diverge already, rendering free-energy convergence on the 100-ns timescale as well as numerical integration of the TI curve difficult. Therefore, an alternative approach was used to calculate ΔG_{con}. PMFs were calculated along a reaction coordinate driving the peptide from the folded to the unfolded state and ΔG_{con} was identified as the free-energy difference between the reaction coordinate values compatible with the conformation pertaining to application of helical dihedral angle restraints (as used in the sampling of PMF2 and M-PMF) and the conformation pertaining to the unrestrained peptide. The reaction coordinate was given by the distance root-mean-square deviation (dRMSD) [56],

$$\mathcal{D}(\{d_i\}) = \sqrt{\frac{1}{N} \sum_{i=1}^{N} \left(d_i - d_{i,0}\right)^2}, \quad (4)$$

the root-mean-square deviation of a set of N distances $\{d_i\}$ with respect to the same set of distances $\{d_{i,0}\}$ in a reference structure. A λ-dependent dRMSD restraining potential

$$V(\lambda; \{d_i\}) = \frac{1}{2} k \left[\mathcal{D}(\{d_i\}) - (1-\lambda)\mathcal{D}_{0,\lambda=0} - \lambda \mathcal{D}_{0,\lambda=1}\right]^2 \quad (5)$$

was used to calculate a PMF along the reaction coordinate $\mathcal{D}(\{d_i\})$ from $\lambda = 0$ to $\lambda = 1$, corresponding to reference dRMSD values of $\mathcal{D}_{0,\lambda=0}$ and $\mathcal{D}_{0,\lambda=1}$, respectively. The range between $\lambda = 0$ and 1 was divided in 16 equidistant PMF windows, eight distances $d_{i,0} = 0.54$ nm between C_α atoms of peptide residues j and $j + 2$, where $j = 3 \ldots 10$ were used to characterize the helical conformation corresponding to $\lambda = 0$ ($\mathcal{D}_{0,\lambda=0} = 0$ nm) and the final state $\lambda = 1$ was set to $\mathcal{D}_{0,\lambda=1} = 0.16$ nm, which implies a fully extended conformation of the peptide. Each PMF window was sampled for 60 ns. PMF calculations were carried out with the peptide in the following environments: (i) in water, (ii) attached to a pure POPC membrane (similar to the bound state in simulation M-PMF), (iii) in the VDAC barrel (similar to the bound state in PMF2) and (iv) in the vicinity of the membrane headgroup region (similar to the region around $z = 2.3 - 2.7$ nm in PMF2). The resulting PMF curves are shown in Fig. S2. To calculate ΔG_{con}, the dRMSD values (Eq. (4) with $d_{i,0}$ set to 0.54 nm for the eight distances between C_α atoms of peptide residues j and $j + 2$, where $j = 3 \ldots 10$) pertaining to peptide conformations with ($\mathcal{D}_f$) and without ($\mathcal{D}_{uf}$) the above helical dihedral angle restraints in the different environments were calculated. Values $\mathcal{D}_f$ and $\mathcal{D}_{uf}$ correspond to local- or near-local minima in the PMFs (Fig. S2). ΔG_{con} is identified as the difference in the associated free energies,

$$\Delta G_{con} = \Delta G(\mathcal{D}_{uf}) - \Delta G(\mathcal{D}_f). \quad (6)$$

From the performed PMF simulations, free energies of binding ΔG_{bnd} were determined as

$$\Delta G_{bnd} = \Delta G_{raw} + \Delta G_{con}(\text{bound}) - \Delta G_{con}(\text{unbound}) + \Delta G_{std}, \quad (7)$$

where the two occurrences of ΔG_{con} (Eq. (6)) refer to the ligand in the bound and unbound state, respectively, and ΔG_{std} is a standard-state correction to allow comparison to experimental data at a concentration of 1 mol L^{-1} for the ligand in the unbound in-solvent state. ΔG_{raw} is given as an exponentional average over the unbound region of the reaction coordinate. Denoting the latter with z,

$$\Delta G_{raw} = \beta^{-1} \ln \int_{unbound} dz \, \exp\left[-\beta \Delta G(z)\right], \quad (8)$$

where the integration is performed in the unbound regime, $\beta = (k_B T)^{-1}$ (k_B being Boltzmann's constant) and $\Delta G(z)$ is the PMF obtained from the WHAM procedure, anchored such that $\Delta G(z)$ vanishes in the bound state [57]. The unbound regime is characterized by negligible interactions between the binding partners. This may be indicated by a plateau in $\Delta G(z)$. For PMF1, no plateau is observed (presumably because increased tension on the NTS causes a very unfavorable strain in the barrel moiety), which is

why here the unbound region was *ad hoc* chosen to be between $z = 3.0$ and $z = 3.7$ nm. For M-PMF, the PMF starts to level off above $z = 3.9$ nm. Although in the investigated distance range above $z = 3.9$ nm, the PMF increases only within $k_B T$, a clear plateau is not reached, presumably because of electrostatic long-range effects. Here, the unbound region was chosen to be between $z = 3.9$ and $z = 4.3$ nm. ΔG_{std} refers to the different volumes available to the ligand in the simulated unbound state V(unbound) and the unbound state at an experimental reference concentration of 1 mol L^{-1}, $V_o = 1.66$ nm^3, [48,57,58]

$$\Delta G_{std} = \beta^{-1} \ln \frac{V_o}{V(\text{unbound})}. \quad (9)$$

It is only added in case of the noncovalent binding reactions, that is, PMF2 and M-PMF, where the unbound state can freely sample a given (box-size and restraining force-constant dependent) in-solvent volume. V(unbound) is given as

$$V(\text{unbound}) = L_x L_y \Delta r_z, \quad (10)$$

where $L_x = L_y$ are the average box-edge lengths along the x- and y-dimensions, respectively, and Δr_z is the distance range along the z-axis sampled by the ligand in an unbound PMF window. Statistical errors on ΔG_{raw} and ΔG_{con} were calculated by adding up the statistical error on the free energies for the bound and unbound state in the former case and for the dRMSD values of the peptide with and without helical restraints in the latter case. The resulting error on ΔG_{bnd} is the sum of the errors on ΔG_{raw} and ΔG_{con}.

For the mutant species V143A and L150A, no PMF calculations were performed. Instead, we reweighted, based on free-energy perturbation [59], the protein configurations of PMF1 to the mutant species using an implicit representation of the solvent and omitting the membrane. This involves three approximations: First, it is assumed that protein configurations sampled in the wild type protein are representative of those sampled in the mutants. Given the small size of the perturbation (replacement of valine and leucine side chains with a methyl group) and the similar chemical nature of initial and perturbed states (nonpolar alkyl side chains), this assumption seems justified. Note that due to the usage of implicit solvent in the reweighting scheme, "holes" in the solvent created by the removal of the valine and leucine side chains that would be present in the original explicit-solvent trajectory do not appear here. Second, it is assumed that the membrane is absent. This is a severe approximation especially considering the fact that the dissociation of the NTS from the barrel involves an intermediate at the membrane surface. However, due to the location of the mutation sites within the barrel rather than in the NTS, we do not expect great artifacts from omission of the membrane and expect artifacts from omitting the membrane to cancel in the considered relative binding free energies (binding free energy in mutants *versus* the wild type). Third, it is assumed that an implicit-solvent representation can capture the relevant free-energetic differences between the wild type protein and the mutants. Implicit solvent models usually give a poor representation of polar solvation due to the neglect of hydrogen bonding, dielectric saturation and electrostriction. Since the mutations considered here only involve nonpolar groups, we expect errors in polar hydration to cancel in the relative binding free energies such that a qualitatively correct picture of the effect of the mutations may be obtained.

In detail, to perform the reweighting, protein configurations were extracted every 40 ps from the first 30 PMF windows, yielding 3250 frames per window. The remaining 18 windows were omitted from the analysis because they involve the steep rise of the PMF associated with pulling the NTS far into the solvent. The free energy of each extracted frame was evaluated with the three protein topologies of interest (wild type, V143A and L150A) based on molecular mechanics—Poisson–Boltzmann surface area (MM-PBSA) calculations. Note that the V143A and L150A topologies essentially involve dummy atoms (exempt of charges and spatial extent) in place of the vanishing valine and leucine atoms and a methyl group at the β-side chain position.

The MM-PBSA free energy of a configuration is a composite of polar (ΔG_{pol}) and apolar (ΔG_{apol}) free-energy contributions, as well as a molecular-mechanical energy term (E_{mm}),

$$\Delta G_{MM-PBSA} = \Delta G_{pol} + \Delta G_{apol} + E_{mm}. \quad (11)$$

The MM-PBSA analysis was done with the gromacs tool g_mmpbsa [60]. The polar energy contribution was calculated with a Poisson–Boltzmann calculation using the APBS solver [61]. Here, relative dielectric permittivities of 1 and 80 were assigned to the solute and solvent moieties, respectively, and the linearized Poisson–Boltzmann equation was solved. The ion density was set to zero. The grid spacing was 0.05 nm and the solute surface was determined by rolling a probe of radius 0.14 nm. Van der Waals radii according to the g_mmpbsa bondi set were used [60]. The apolar energy contribution was calculated based on the solvent accessible surface area, using a probe radius of 0.14 nm, a surface tension coefficient of 2.26778 kJ mol^{-1} nm^{-2} and an offset of 3.84928 kJ mol^{-1}. Molecular-mechanical energy contributions were calculated based on the force field employed during the simulations (MD simulations section).

Using the quantities $\Delta G^{wt}_{MM-PBSA}$ and $\Delta G_{MM-PBSA}{}^{mut}$ pertaining to the wild type and a mutant species, respectively, the probability of a sampled wild type configuration i in PMF window j reweighted to a mutant is [59].

$$p^{rew}_{i,j} = \exp\left[-\frac{\Delta G^{mut}_{MM-PBSA} - \Delta G^{wt}_{MM-PBSA}}{k_B T}\right]. \quad (12)$$

The reweighted probabilities for all extracted configurations i in PMF windows j were used to construct reweighted reaction-coordinate probability distributions per PMF window, that is, the reweighted probability of distance bin k in PMF window j is

$$p^{rew}_{k,j} = \sum_{i=1}^{N_j} \delta_k p^{rew}_{i,j}, \quad (13)$$

where i runs over frames, $N_j = 3250$ is the number of frames per PMF window j and $\delta_k = 1$ if the reaction-coordinate value of frame i is in bin k, whereas otherwise $\delta_k = 0$. The bin width was set to 0.01 nm. The reweighted distributions $p^{rew}_{k,j}$ of each PMF window j were normalized, and the WHAM algorithm [49,50] was used to construct a corresponding reweighted PMF with a bin width 0.01 nm. The resulting PMFs were slightly smoothened by averaging over five consecutive points.

Analysis of simulations

The stability of the proteins during the simulations was assessed by monitoring the time series of the atom-positional rmsd of all backbone atoms (N, C_α, C) from the energy-minimized x-ray structure (PDB ID 3EMN) after a roto-translational fit of all backbone atoms to this (reference) structure and by monitoring the occurrence of secondary structure elements α-helix, 3_{10}-helix, π-helix or β-sheet based on secondary structure definitions according to the Kabsch–Sander rules (dssp) [62].

The local backbone flexibility of the proteins during the simulations was assessed by calculating the atom-positional root-mean-square fluctuation (rmsf) for all C_α atoms, after a roto-translational fit of all backbone atoms to the energy-minimized structure. Hydrogen bonds were analyzed *via* a geometric detection criterion (donor–hydrogen–acceptor angle larger than 135 deg. and hydrogen–acceptor distance smaller than 0.25 nm). Barrel shape was characterized by least squares fitting of an ellipse [63] to the set of data points given by those C_α atoms in the β-strands whose z-coordinate lies within $z_m \pm \delta$, where z_m is the mean of the minimum and maximum z-coordinate of all β-strand C_α atoms in a given frame. The parameter δ was set to 0.15 nm, leading to 21.1 data points (C_α atoms) on average, with a standard deviation of 1.7. This allows a meaningful fit of an ellipse to the 19-stranded β-barrel. The ellipse is described by the lengths of the semi-major and semi-minor axes, a and b, respectively, and the angle φ enclosed by the former and the x-axis. Furthermore, barrel shape changes during NTS dissociation were analyzed in terms of backbone atom-positional rmsd from the energy-minimized x-ray structure (PDB ID 3EMN) after a roto-translational fit of all backbone atoms to this (reference) structure and in terms of mass-weighted radius of gyration of barrel backbone atoms. In both of the latter analyses, only residues 27–283 were considered to capture the pore only and exclude the protruding NTS.

Simulations M-NTS1–M-NTS4 were analyzed with respect to the interaction of the peptide with the membrane and the positioning of the peptide along the membrane. We calculated (i) the secondary structure content according to the Kabsch–Sander rules [62]; (ii) the atom-positional rmsf for all C_α atoms, after a roto-translational fit of all backbone atoms to the first trajectory frame; (iii) conformation- and position-based similarity matrices, where conformational similarity was estimated by means of the atom-positional rmsd between backbone atoms and positional similarity was estimated by means of the rmsd between either of the following per-residue properties: the angle between the z-axis and the vector pointing from the com to the C_α atom of the residue or the height of the residue com below the plane containing the membrane com. Based on these similarity criteria, clustering was conducted for peptide–membrane configurations extracted every 100 ps from the trajectories of simulations M-NTS1–4, that is, a pool of 16,000 configurations. The rmsd cutoffs for the three above clusterings were set to 0.24 nm, 35 deg. and 0.25 nm, respectively. In the latter case, this corresponds to a shoulder in the pairwise rmsd distribution. In the two former cases, it is close to the position of the local minimum in the distribution, shifted slightly toward the right such that the first three clusters contain between 60% and 70% of all structures. In the three above clusterings, this fraction is 69%, 69% and 65%. Clusters were defined such that all configurations pertaining to a particular cluster be within the given rmsd cutoff distance of the central member structure of the cluster [64].

Visual analyses were done with the programs vmd [41] (version 1.9.1) and PyMOL [65] (version 1.7.0). Computational analyses were done with the gromacs 5.1.2 program package [29,30], except for hydrogen-bond and cluster analyses, which were done with the gromos++ program package [32].

VDAC NTS production in *Escherichia coli* for NMR

The ^{15}N-labeled VDAC NTS (residues 1 to 26) was produced as a fusion construct with an N-terminal

protein G B1 domain (GB1), a tobacco etch virus (TEV) protease cleavage site and an N-terminal His6-tag [66]. One liter of M9 minimal medium [67] supplemented with 100 mg L^{-1} ampicillin and containing 1 g per liter of ^{15}N-labeled ammonium chloride (Sigma-Aldrich) was inoculated with an overnight culture in a 1:50 ratio, and protein production was induced at an OD600 of 0.75 by the addition of 1 mM IPTG. After further shaking for 4 h at 37 °C, cells were harvested by centrifugation (8000*g*, 30 min, 4 °C) and stored at −80 °C for further use. Cells were thawn and resuspended in 25 mL buffer containing 20 mM NaPi (pH 7.0), 50 mM NaCl and 0.5 mM EDTA (buffer A). Subsequently, 0.2 mg mL^{-1} Lysozyme, 100 U DNAseI and one tablet of Complete EDTA-free protease inhibitor (Roche) were added. After incubation for 30 min on ice, cell breakage was done by sonication (1-s pulse and 2-s pause, 30% amplitude, total pulse time: 10 min). Cell debris was spun down for 30 min at 60,000*g* and 4 °C and the supernatant was subsequently applied to a Ni-NTA affinity column equilibrated with buffer A without EDTA. The closed column was shaken at 4 °C for 60 min to maximize protein binding to the affinity resin. The column was then washed with buffer A containing 10 mM imidazole, and the protein was eluted with 400 mM imidazole in buffer A and dialyzed into buffer A containing 2 mM DTT. To cleave off the GB1 tag, TEV protease (1 mg) was added to the protein and incubated overnight at room temperature, followed by reverse Ni-NTA to separate hVADC1-N from GB1 and TEV protease. The flow-through and wash fractions were collected and concentrated using a 1-kDa MWCO spin concentrator (EMDMillipore).

Assembly of nanodiscs containing *E. coli* total lipids

Empty nanodiscs were assembled with MSP1D1 [68] according to established protocols [69,70] using *E. coli* total lipids (Avanti Polar Lipids) [50 mM lipids in 100 mM cholate, 20 mM Tris/HCl (pH 7.5), 100 mM NaCl, 0.5 mM EDTA] using a 1:55 MSP-to-lipid ratio. Incubation of the assembly mix was performed at room temperature for 60 min followed by the addition of 0.6 g/mL Biobeads-SM2 (Bio-Rad) to initiate nanodisc assembly by detergent removal for 90 min on a shaker platform at room temperature. Finally, gel filtration on a Superdex-200 (GE Healthcare) column was performed in buffer A, and protein-containing fractions were collected and concentrated to 600 μM.

NMR titrations

All TROSY spectra [71] were collected on a Bruker Avance-III NMR spectrometer operating at 950 MHz proton frequency and equipped with a cryogenic probe. Data processing was performed with Topspin3.5 (Bruker Biospin), and spectral analysis was done with SPARKY [72]. All experiments were performed at 298 K with 32 scans and 1024 and 128 complex points in the direct (^{1}H) and indirect (^{15}N) dimension, respectively. First, as a reference, a spectrum of 200 μM ^{15}N-labeled VDAC NTS in buffer A and 5% (v/v) D_2O was recorded, followed by 100 μM VDAC NTS in the presence of 500 μM of empty MSP1D1 nanodiscs containing *E. coli* total lipids. CSPs were extracted according to established protocols [73] and visualized with UCSF-Chimera [28].

Acknowledgments

Computer resources for this project were provided by the Gauss Centre for Supercomputing/Leibniz Supercomputing Centre under Grant pr48po.

Appendix A. Supplementary data

Supplementary data to this article contain further details of the VDAC system, dRMSD calculations, structural analyses of VDAC and the NTS-derived peptide and of MM-PBSA end point binding free-energy calculations. Supplementary data to this article can be found online at https://doi.org/10.1016/j.jmb.2018.09.015.

Received 26 June 2018;
Received in revised form 11 September 2018;
Accepted 26 September 2018
Available online 17 October 2018

Keywords:
voltage-dependent anion channel;
N-terminal helix;
potential of mean force;
membrane binding;
chemical shift perturbations

Abbreviations used:
VDAC, voltage-dependent anion channel; NTS, N-terminal segment; OMM, outer mitochondrial membrane; PMF, potential of mean force; HRE, Hamiltonian Replica Exchange; TI, thermodynamic integration; dRMSD, distance root-mean-square deviation; CSP, chemical shift perturbation.

References

[1] V. De Pinto, S. Reina, F. Guarino, A. Messina, Structure of the voltage dependent anion channel: state of the art, J. Bioenerg. Biomembr. 40 (2008) 139–147.
[2] V. Shoshan-Barmatz, V. De Pinto, M. Zweckstter, Z. Raviv, N. Keinan, N. Arbel, VDAC, a multi-functional mitochondrial protein regulating cell life and death, Mol. Asp. Med. 31 (2010) 227–285.

[3] O.P. Choudhary, R. Ujwal, W. Kowallis, R. Coalson, J. Abramson, M. Grabe, The electrostatics of VDAC: implications for selectivity and gating, J. Mol. Biol. 396 (2010) 580–592.
[4] S. Geula, D. Ben-Hail, V. Shoshan-Barmatz, Structure-based analysis of VDAC1: N-terminus location, translocation, channel gating and association with anti-apoptotic proteins, Biochem. J. 444 (2012) 475–485.
[5] S.Y. Noskov, T.K. Rostovtseva, A.C. Chamberlin, O. Teijido, W. Jiang, S.M. Bezrukov, Current state of theoretical and experimental studies of the voltage-dependent anion channel (VDAC), Biochim. Biophys. Acta 1858 ((2016) 1778–1790.
[6] B. O'Rourke, S. Cortassa, M.A. Aon, Mitochondrial ion channels: gatekeepers of life and death, Physiology (Bethesda) 20 (2005) 303–315.
[7] B. O'Rourke, Mitochondrial ion channels, Annu. Rev. Physiol. 69 (2007) 19–49.
[8] Y. Chu, J.G. Goldman, L. Kelly, Y. He, T. Waliczek, J.H. Kordower, Abnormal alpha-synuclein reduces nigral voltage-dependent anion channel 1 in sporadic and experimental Parkinson's disease, Neurobiol. Dis. 69 (2014) 1–14.
[9] V. Shoshan-Barmatz, D. Ben-Hail, L. Admoni, Y. Krelin, S.S. Tripathi, The mitochondrial voltage-dependent anion channel 1 in tumor cells, Biochim. Biophys. Acta 1848 ((2015) 2547–2575.
[10] M. Colombini, Voltage gating in the mitochondrial channel, VDAC, J. Membr. Biol. 111 (1989) 103–111.
[11] R. Ujwal, D. Cascio, J.P. Colletier, S. Faham, J. Zhang, L. Toro, P. Ping, J. Abramson, The crystal structure of mouse VDAC1 at 2.3 Å resolution reveals mechanistic insights into metabolite gating, Proc. Natl. Acad. Sci. U. S. A. 105 (2008) 17742–17747.
[12] S. Hiller, R.G. Garces, T.J. Malia, V.Y. Orekhov, M. Colombini, G. Wager, Solution structure of the integral human membrane protein VDAC-1 in detergent micelles, Science 321 (2008) 1206–1210.
[13] X.W. Guo, P.R. Smith, B. Cognon, D. D'Arcangelis, E. Dolginova, C.A. Mannella, Molecular design of the voltage-dependent, anion-selective channel in the mitochondrial outer membrane, J. Struct. Biol. 114 (1995) 41–59.
[14] R. Schneider, M. Etzkorn, K. Giller, V. Daebel, J. Eisfeld, M. Zweckstetter, C. Griesinger, S. Becker, A. Lange, The native conformation of the human VDAC1 N-terminus, Angew. Chem. Int. Ed. Engl. 49 (2010) 1882–1885.
[15] V. De Pinto, F. Tomasello, A. Messina, F. Guarino, R. Benz, D. La Mendola, A. Magri, D. Milardi, G. Pappalardo, Determination of the conformation of the human VDAC1 N-terminal peptide, a protein moiety essential for the functional properties of the pore, Chembiochem 8 (2007) 744–756.
[16] S.R. Shuvo, F.G. Ferens, D.A. Court, The N-terminus of VDAC: structure, mutational analysis and a potential role in regulating barrel shape, Biochim. Biophys. Acta 1858 (2016) 1350–1361.
[17] B. Mertins, G. Psakis, W. Grosse, K.C. Back, A. Salisowski, P. Reiss, U. Koert, L.O. Essen, Flexibility of the N-terminal mVDAC1 segment controls the channel's gating behavior, PLoS One 7 (2012) e47939/1–e47939/14.
[18] S. Reymann, H. Florke, M. Heiden, C. Jakob, U. Stadtmuller, P. Steinacker, V.E. Lalk, I. Pardowitz, F.P. Thinnes, Further evidence for multitopological localization of mammalian porin (VDAC) in the plasmalemma forming part of a chloride channel complex affected in cystic fibrosis and encephalomyopathy, Biochem. Mol. Med. 54 (1995) 75–87.
[19] L. Thomas, E. Blachly-Dyson, M. Colombini, M. Forte, Mapping of residues forming the voltage sensor of the voltage-dependent anion-selective channel, Proc. Natl. Acad. Sci. U. S. A. 90 (1993) 5446–5449.
[20] S. Abu-Hamad, N. Arbel, D. Calo, L. Arzoine, A. Israelson, N. Keinan, R. Ben-Romano, O. Friedman, V. Shoshan-Barmatz, The VDAC1 N-terminus is essential both for apoptosis and the protective effect of anti-apoptotic proteins, J. Cell Sci. 122 (2009) 1906–1916.
[21] R. Briones, C. Weichbrodt, L. Paltrinieri, I. Mey, S. Villinger, K. Giller, A. Lange, M. Zweckstetter, C. Griesinger, S. Becker, C. Steinem, B.L. de Groot, Voltage dependence of conformational dynamics and subconducting states of VDAC-1, Biophys. J. 111 (2016) 1223–1234.
[22] O. Teijido, R. Ujwal, C.O. Hillderdal, L. Kullman, T.K. Rostovtseva, J. Abramson, Affixing N-terminal alpha-helix to the wall of the voltage-dependent anion channel does not prevent its voltage gating, J. Biol. Chem. 287 (2012) 11437–11445.
[23] U. Zachariae, R. Schneider, R. Briones, Z. Gattin, J.P. Demers, K. Giller, E. Maier, M. Zweckstetter, C. Griesinger, S. Becker, R. Benz, B.L. de Groot, A. Lange, Beta-barrel mobility underlies closure of the voltage-dependent anion channel, Structure 20 (2012) 1540–1549.
[24] T.K. Rostovtseva, N. Kazemi, M. Weinrich, S.M. Bezrukov, Voltage gating of VDAC is regulated by nonlamellar lipids of mitochondrial membranes, J. Biol. Chem. 281 (2006) 37496–37506.
[25] T.K. Rostovtseva, S.M. Bezrukov, VDAC regulation: role of cytosolic proteins and mitochondrial lipids, J. Bioenerg. Biomembr. 40 (2008) 163–170.
[26] O.P. Choudhary, A. Paz, J.L. Adelman, J.-P. Colletier, J. Abramson, M. Grabe, Structure-guided simulations illuminate the mechanism of ATP transport through VDAC1, Nat. Struct. Mol. Biol. 21 (2014) 626–634.
[27] S. Villinger, R. Briones, K. Giller, U. Zachariae, A. Lange, B.L. de Groot, C. Griesinger, S. Becker, M. Zweckstetter, Functional dynamics in the voltage-dependent anion channel, Proc. Natl. Acad. Sci. U. S. A. 107 (2010) 22546–22551.
[28] E.F. Pettersen, T.D. Goddard, C.C. Huang, G.S. Couch, D.M. Greenblatt, E.C. Meng, T.E. Ferrin, UCSF Chimera—a visualization system for explanatory research and analysis, J. Comput. Chem. 25 (2004) 1605–1612.
[29] D. van der Spoel, E. Lindahl, B. Hess, G. Groenhof, A.E. Mark, H.J.C. Berendsen, GROMACS: fast, flexible, and free, J. Comput. Chem. 26 (2005) 1701–1718.
[30] B. Hess, C. Kutzner, D. van der Spoel, E. Lindahl, GROMACS 4: algorithms for highly efficient, load-balanced, and scalable molecular simulation, J. Chem. Theory Comput. 4 (2008) 435–447.
[31] G.A. Tribello, M. Bonomi, D. Branduardi, C. Camilloni, G. Bussi, PLUMED 2: new feathers for an old bird, Comput. Phys. Commun. 185 (2014) 604–613.
[32] A.P. Eichenberger, J.R. Allison, J. Dolenc, D.P. Geerke, B.A. C. Horta, K. Meier, C. Oostenbrink, N. Schmid, D. Steiner, D. Wang, W.F. van Gunsteren, The GROMOS++ software for the analysis of biomolecular simulation trajectories, J. Chem. Theory Comput. 7 (2011) 3379–3390.
[33] N. Schmid, A.P. Eichenberger, A. Choutko, S. Riniker, M. Winger, A.E. Mark, W.F. van Gunsteren, Definition and testing of the GROMOS force-field versions 54A7 and 54B7, Eur. Biophys. J. 40 (2011) 843–856.
[34] H.J.C. Berendsen, J.P.M. Postma, W.F. van Gunsteren, A. di Nola, J.R. Haak, Molecular dynamics with coupling to an external bath, J. Chem. Phys. 81 (1984) 3684–3690.
[35] B. Hess, H. Bekker, H.J.C. Berendsen, J.G.E.M. Fraaije, LINCS: a linear constraint solver for molecular simulations, J. Comput. Chem. 18 (1997) 1463–1472.

[36] R.W. Hockney, The potential calculation and some applications, Methods Comput. Phys. 9 (1970) 135–211.
[37] J.A. Barker, R.O. Watts, Monte Carlo studies of the dielectric properties of water-like models, Mol. Phys. 26 (1973) 789–792.
[38] T.N. Heinz, W.F. van Gunsteren, P.H. Hünenberger, Comparison of four methods to compute the dielectric permittivity of liquids from molecular dynamics simulations, J. Chem. Phys. 115 (2001) 1125–1136.
[39] M.M. Reif, C. Kallies, V. Knecht, Effect of sodium and chloride binding on a lecithin bilayer. A molecular dynamics study, Membranes 7 (2017) 5/1–5/22.
[40] A.K. Malde, L. Zuo, M. Breeze, M. Stroet, D. Poger, P.C. Nair, C. Oostenbrink, A.E. Mark, An automated force field topology builder (ATB) and repository: version 1.0, J. Chem. Theory Comput. 7 (2011) 4026–4037.
[41] W. Humphrey, A. Dalke, K. Schulten, VMD—visual molecular dynamics, J. Mol. Graph. 14 (1996) 33–38.
[42] H.J.C. Berendsen, J.P.M. Postma, W.F. van Gunsteren, J. Hermans, Interaction models for water in relation to protein hydration, in: B. Pullman (Ed.), Intermolecular Forces, Reidel, Dordrecht, The Netherlands 1981, pp. 331–342.
[43] Y. Sugita, A. Kitao, Y. Okamoto, Multidimensional replica-exchange method for free-energy calculations, J. Chem. Phys. 113 (2000) 6042–6051.
[44] H. Fukunishi, O. Watanabe, S. Takada, On the Hamiltonian replica exchange method for efficient sampling of biomolecular systems: application to protein structure prediction, J. Chem. Phys. 116 (2002) 9058–9067.
[45] R. Affentranger, I. Tavernelli, E.E. di Iorio, A novel hamiltonian replica exchange MD protocol to enhance protein conformational space sampling, J. Chem. Theory Comput. 2 (2006) 217–228.
[46] H.-J. Woo, B. Roux, Calculation of absolute protein–ligand binding free energy from computer simulations, Proc. Natl. Acad. Sci. U. S. A. 102 (2005) 6825–6830.
[47] J.C. Gumbart, B. Roux, C. Chipot, Efficient determination of protein–protein standard binding free energies from first principles, J. Chem. Theory Comput. 9 (2013) 3789–3798.
[48] J.W. Perthold, C. Oostenbrink, Simulation of reversible protein–protein binding and calculation of binding free energies using perturbed distance restraints, J. Chem. Theory Comput. 13 (2017) 5697–5708.
[49] S. Kumar, D. Bouzida, R.H. Swendsen, P.A. Kollman, J.M. Rosenberg, The weighted histogram analysis method for free-energy calculations on biomolecules. I. The method, J. Comput. Chem. 13 (1992) 1011–1021.
[50] B. Roux, The calculation of the potential of mean force using computer simulation, Comput. Phys. Commun. 91 (1995) 275–282.
[51] A. Grossfield, The Weighted Histogram Analysis Method. Version 2.0.9, Available at: http://membrane.urmc.rochester.edu/content/wham 2013.
[52] J.G. Kirkwood, Quantum statistics of almost classical assemblies, Phys. Rev. 44 (1933) 31–37.
[53] J.G. Kirkwood, Quantum statistics of almost classical assemblies, Phys. Rev. 45 (1934) 116–117.
[54] M. Christen, A.-P.E. Kunz, W.F. van Gunsteren, Sampling of rare events using hidden restraints, J. Phys. Chem. B 110 (2006) 8488–8498.
[55] M. Christen, A.-P.E. Kunz, W.F. van Gunsteren, Erratum to: "Sampling of rare events using hidden restraints" [J. Phys. Chem. B 110, 8488–8498 (2006)], J. Phys. Chem. B 112 (2008) 11446.
[56] M.P. Luitz, R. Bomblies, E. Ramcke, A. Itzen, M. Zacharias, Adenylylation of Tyr77 stabilizes Rab1b GTPase in an active state: a molecular dynamics simulation analysis, Sci. Rep. 6 (2016) 19896/1–19896/11.
[57] S. Doudou, N.A. Burton, R.H. Henchman, Standard free energy of binding from a one-dimensional potential of mean force, J. Chem. Theory Comput. 5 (2009) 909–918.
[58] G. Nagy, C. Oostenbrink, J. Hritz, Exploring the binding pathways of the 14-3-3ζ protein: structural and free-energy profiles revealed by Hamiltonian replica exchange molecular dynamics with distancefield distance restraints, PLoS One 12 (2017) e0180633/1–e0180633/30.
[59] R.W. Zwanzig, High-temperature equation of state by a perturbation method. I. Nonpolar gases, J. Chem. Phys. 22 (1954) 1420–1426.
[60] R. Kumari, R. Kumar, Lynn Open Source Drug Discovery Consortium, g_mmpbsa—A GROMACS tool for high-throughput MM-PBSA calculations, J. Chem. Inf. Model. 54 (2014) 1951–1962.
[61] N.A. Baker, D. Sept, S. Joseph, M.J. Holst, J.A. McCammon, Electrostatics of nanosystems: application to microtubules and the ribosome, Proc. Natl. Acad. Sci. U. S. A. 98 (2001) 10037–10041.
[62] W. Kabsch, C. Sander, Dictionary of protein secondary structure: pattern recognition of hydrogen-bonded and geometrical features, Biopolymers 22 (1983) 2577–2637.
[63] A. Fitzgibbon, M. Pilu, R.B. Fisher, Direct least square fitting of ellipses, IEEE Trans. Pattern Anal. Mach. Intell. 21 (1999) 476–480.
[64] X. Daura, W.F. van Gunsteren, A.E. Mark, Folding-unfolding thermodynamics of a β-heptapeptide from equilibrium simulations, Proteins Struct. Funct. Genet. 34 (1999) 269–280.
[65] W.L. Delano, The PyMOL Molecular Graphics System, Available at http://www.pymol.org 2002.
[66] P. Zhou, G. Wagner, Overcoming the solubility limit with solubility-enhancement tags: successful applicatios in biomolecular NMR studies, J. Biomol. NMR 46 (2010) 23–31.
[67] J. Sambrook, D.W. Russell, Molecular Cloning: A Laboratory Manual, Cold Spring Harbor Laboratory, Cold Spring Harbor, N.Y. USA2001.
[68] I.G. Denisov, Y.V. Grinkova, A.A. Lazarides, S.G. Sligar, Directed self-assembly of monodisperse phospholipid bilayer nanodiscs with controlled size, J. Am. Chem. Soc. 126 (2004) 3477–3487.
[69] F. Hagn, M. Etzkorn, T. Raschle, G. Wagner, Optimized phospholipid nanodiscs facilitate high-resolution structure determination of membrane proteins, J. Am. Chem. Soc. 135 (2013) 1919–1925.
[70] F. Hagn, M.L. Nasr, G. Wagner, Assembly of phospholipid nanodiscs of controlled size for structural studies of membrane proteins by NMR, Nat. Protoc. 13 (2018) 79–98.
[71] K. Pervushin, R. Riek, G. Wider, K. Wüthrich, Attenuated T2 relaxation by mutual cancellation of dipole-dipole coupling and chemical shift anisotropy indicates an avenue to NMR structures of very large biological macromolecules in solution, Proc. Natl. Acad. Sci. U. S. A. 94 (1997) 12366–12371.
[72] T.D. Goddard, D.G. Kneller, SPARKY, University of California, San Francisco, Available at: https://www.cgl.ucsf.edu/home/sparky/ 2004.
[73] F. Hagn, C. Klein, O. Demmer, N. Marchenko, A. Vaseva, U. M. Moll, H. Kessler, Bcl-x_L changes conformation upon binding to wild-type but not mutant p53 DNA binding domain, J. Biol. Chem. 285 (2010) 3439–3450.